

In-silico molecular transport via perivascular networks in the human intracranial space

Marius Causemann¹, Miroslav Kuchta¹, Rami Masri², and Marie E. Rognes^{1,3,*}

¹Department of Numerical Analysis and Scientific Computing, Simula Research Laboratory, Oslo, Norway

²Division of Applied Mathematics, Brown University, Providence, Rhode Island, USA

³K. G. Jebsen Centre for Brain Fluid Research, University of Oslo, Norway

*meg@simula.no

ABSTRACT

The mechanisms of intracranial solute transport are fundamental to human brain health, with alterations often linked to disease and functional impairment, and with distinct opportunities for personalized diagnostics and treatment. However, our understanding of these mechanisms and their interplay remains incomplete, in part due to the complexity of integrating insights across scales, between species and from different modalities. Here, we combine mixed-dimensional modelling, multi-modal magnetic resonance images, and high performance computing to construct and explore a high-fidelity in-silico model of human intracranial molecular transport. This model predicts the temporo-spatial spreading of a solute within an image-derived geometric representation of the subarachnoid space, ventricular system and brain parenchyma, including networks of surface perivascular spaces (PVSs). Our findings highlight the significant impact of cerebrospinal fluid (CSF) production and intracranial pulsatility on tracer enrichment following intrathecal tracer injection. We demonstrate that low-frequency vasomotion induces moderate CSF flow in surface PVS networks which substantially enhances tracer enrichment, and that impaired enrichment is a direct natural consequence of enlarged surface PVSs. This openly available technology platform thus provides an opportunity for integrating separate observations on diffusion in neuropil, vascular dynamics, intracranial pulsatility, CSF production, and efflux, and for exploring drug delivery and clearance in the human brain.

Introduction

The mechanisms underlying molecular transport within the intracranial space are fundamental to human brain health and function. Neurodegenerative diseases such as Alzheimer's, Parkinson's, and Huntington's disease are all associated with abnormal accumulation of protein aggregates together with alterations in transport and clearance characteristics^{1–4}. Moreover, sleep and conversely sleep-deprivation play a definite yet enigmatic role in modulating molecular transport and clearance^{5–9}. In the last decade, established theories have been challenged by new findings on molecular movement and exchange^{10–14}, including substantial variability between individuals and between patient cohorts^{7, 15–17}. These observations provide distinct opportunities (and challenges) for personalized medicine e.g. for tailored intrathecal delivery of chemotherapies¹⁸ such as methotrexate in acute lymphoblastic leukemia patients¹⁹, and for early diagnostics of impaired brain clearance^{20, 21}. In spite of their importance, our understanding of these mechanisms is incomplete with open challenges and significant debate – in part relating to the translation of knowledge between scales, species, experimental protocols, clinical cohorts, and individuals.

Perivascular pathways along the brain surface and within the brain parenchyma have long been hypothesized to serve a designated role in this context^{10, 22–28}. Recently, Eide and Ringstad²⁹ and Yamamoto et al³⁰ demonstrated that perivascular spaces (PVSs) define preferential pathways for molecular transport in humans, with delayed periarterial enrichment in dementia subtypes²⁹. Perivascular flow of cerebrospinal fluid (CSF) clearly contributes to this transport, and is inherently associated with vascular pulsations^{31–36}. Fluid mechanics considerations point at intracranial pressure differences and shorter wavelength vascular wall pulsations as drivers of directional net flow and convection in the PVS^{37–42}, while longer waves such as the pulse wave primarily contribute to oscillatory flow and dispersion^{43–48}. In the bigger picture, CSF is produced by the choroid plexus^{49–51}, pulsates through the ventricular system, cisterns, and subarachnoid space (SAS) in association with cardiac, respiratory, and neural waves^{16, 52–59}, and drains via the dural sinuses, meningeal lymphatics, cranial nerves, or other efflux pathways¹³. However, how these physiological factors and physical mechanisms integrate to enhance or impair human intracranial molecular transport over larger spatial scales and longer time scales remain unknown. A related key question is to what extent surface PVSs are separated from the SAS by structural barriers^{23, 29, 60–65}, and in turn to what extent such structural compartmentalization is a prerequisite for effective perivascular transport.

In this study, by leveraging geometric model reduction and mixed-dimensional modelling⁶⁶, structural magnetic resonance (MR) images⁶⁷, and high performance computing, we introduce an integrated computational model of intracranial molecular

36 transport. Focusing on the interplay between perivascular pathways, pulsatility and CSF flow dynamics, the model predicts the
37 temporal evolution and spatial distribution of a solute concentration within a detailed geometric representation of the human
38 SAS and ventricular system, in networks of surface PVSs (i.e. those surrounding arteries and veins in the SAS), and in the brain
39 parenchyma. In terms of transport dynamics, we account for heterogeneous diffusion, dispersive mixing induced by cardiac and
40 respiratory pulsatility in the CSF spaces and PVSs, convective fluid flow driven by CSF production and peristaltic pumping, as
41 well as solute exchange and clearance across semi-permeable membranes. Comparing with glymphatic MRI studies^{11,15,29,68},
42 the in-silico predictions accurately represent tracer enrichment patterns, timing and intercompartmental distributions. This open
43 platform⁶⁹ thus provides a technological opportunity for qualitatively and quantitatively exploring key open questions relating
44 to molecular movement within the human brain environment such as the role of pulsatility, perivascular pathways, structural
45 compartmentalization, or morphology.

46 By exploring this high-dimensional parameter space, we propose that the balance between CSF production and intracranial
47 pulsatility is key to shaping the large-scale features of intracranial enrichment patterns, with the potential to span a wide
48 range of individual and cohort variability. Moreover, we predict that CSF production, cardiac- and respiratory pulsatility is
49 not sufficient to explain early perivascular enrichment, but that fluid flow induced by low-frequency vasomotion in surface
50 periarterial spaces (on the order of 10 μm/s) is sufficient, even in the absence of a structural compartmentalization of the PVS.
51 Conversely, enlarged PVSs in the SAS will cause a substantial reduction in cardiac- and vasomotion-driven flow velocities,
52 strongly delay perivascular transport, and thus impair intracranial enrichment. These findings transfer, reconcile, integrate and
53 extend insights from clinical, experimental, and theoretical studies, and provide a framework for future in-silico studies of
54 personalized intrathecal drug delivery and brain clearance.

55 Results

56 In-silico predictions of intracranial transport after intrathecal injection

57 Using previously published multi-modal magnetic resonance imaging (MRI) data^{67,70–73}, we construct a multiscale com-
58 putational representation of the human intracranial compartments consisting of the CSF spaces and brain parenchyma as
59 three-dimensional (3D) domains and with the PVSs surrounding major surface arteries and veins as embedded networks of
60 topologically one-dimensional (1D) curves (Figure 1A–B). We consider a solute concentration field, varying in space and
61 time, in the 3D domains and in the PVS networks, and assume that the solute can cross between these compartments through
62 semi-permeable membranes. As the drivers and modes of intracranial transport are under substantial debate^{13,14,74–76}, our first
63 target is to establish a baseline model accounting for a reasonably conservative set of mechanisms and their integrated effect
64 over a timescale of several minutes to a few days. To this end, we assume that the solute will (i) diffuse within all compartments,
65 with diffusivity depending on the effective properties of the relevant medium⁷⁷; (ii) experience significant dispersive effects
66 due to the pulsatile flow of CSF induced by the cardiac and respiratory cycles^{44,47,56,78}; and (iii) be convected by a (small)
67 net flow of CSF resulting from production in the choroid plexus with CSF efflux across the upper convexity⁷⁹ and from the
68 peristaltic pumping effect of pulse wave pulsations in surface periarterial spaces^{34,41}. Mathematically, this model is represented
69 by a mixed-dimensional system of coupled time-dependent partial differential equations⁶⁶, which we solve numerically with
70 high accuracy using a mass-conserving finite element scheme and the FEniCS finite element software^{80,81} (see Methods). The
71 computational framework and associated software are all openly available⁶⁹.

72 Simulating a glymphatic MRI protocol^{11,15,29} (Figure 1C), we then predict the spreading of 0.5 mmol intrathecally injected
73 Gadobutrol after its appearance at the craniocervical junction, represented by tracer inflow across the spinal SAS boundary over
74 the first two hours (Figure 1D–E). After one hour, the in-silico tracer moves upwards in the SAS frontally of the brainstem, and
75 quickly reaches the supratentorial regions. Here, it spreads both posterior through the quadrigeminal cistern and the longitudinal
76 fissure, and anteriorly through the outer SAS, reaching the top of the cerebral cortex after around 12 hours. After 24 hours,
77 the tracer covers most of the brain surface (with the exception of some posterior regions) and has penetrated substantially
78 into the parenchymal tissue. This pattern is reflected in the mean tracer concentrations in each compartment, where the CSF
79 space reaches its peak of 1.4 mmol/l after 2 hours, followed by the arterial PVS concentration peak (2.9 mmol/l after 4 hours)
80 (Figure 1F). While the mean concentrations in these compartments drop soon after peaking, the parenchymal tissue slowly
81 enriches with tracer over the first 24 hours, with a final value of 0.3 mmol/l. Overall, about 40% of the total amount of tracer
82 remains in the cranium 24 hours post-injection, with the largest share in the CSF (53%), followed by the parenchyma (35%),
83 the venous PVS (8%) and the arterial PVS (5%) (Figure 1G).

84 Reduced CSF pulsatility strongly shifts intracranial enrichment patterns

85 The tracer enrichment patterns observed clinically after intrathecal injection of contrast differ substantially between subjects
86 and between pathological conditions^{7,15–17}. These neurological conditions are also associated with alterations in the pulsatile
87 flow of CSF in the ventricular system and SAS¹⁶. Clearly, key physiological factors such as cardiac pulsatility and respiration

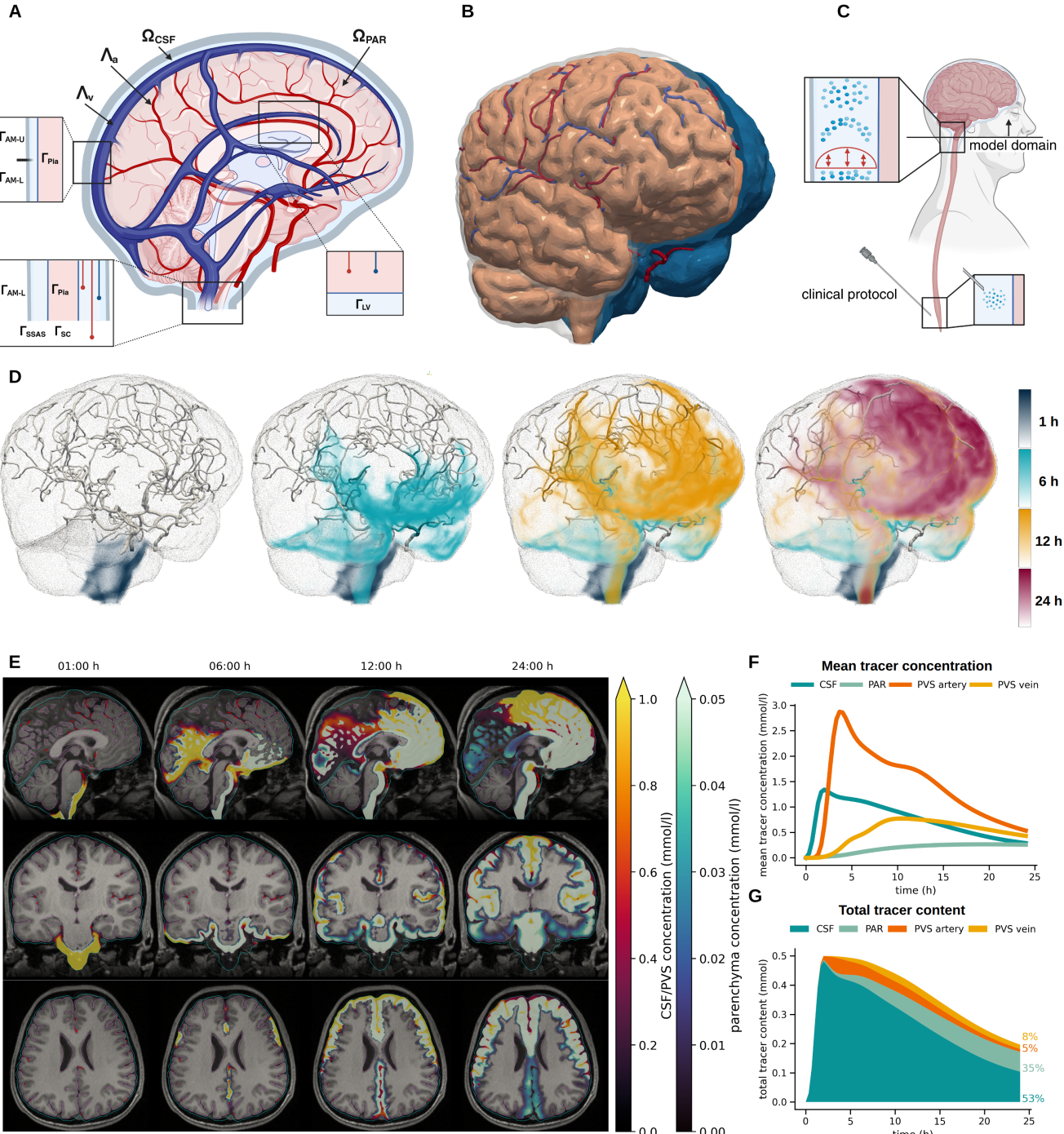


Figure 1. In-silico modelling of tracer transport in the PVS, SAS and parenchyma. A) Illustration of the model geometry including the CSF-filled spaces (Ω_{CSF}), the parenchyma (Ω_{PAR}) and the PVS surrounding arteries Λ_{artery} and veins Λ_{vein} , as well as their interfaces and boundaries; B) 3D rendering of the computational geometry: the parenchyma, CSF (clipped, blue), arterial network (red), and venous network (blue); C) illustration of the intrathecal tracer injection protocol; D) in-silico predictions of tracer concentration after 1, 6, 12, and 24 hours (opacity increasing linearly from 0 to 2 mmol/l); E) sagittal, coronal and axial view of in-silico tracer concentrations overlayed on T1-weighted MR image after 1, 6, 12 and 24 h (low concentrations transparent, pial surface in pink, arachnoid membrane in cyan, and arteries in dark red); F) average tracer concentration in each compartment over the first 24 h; G) total amount of tracer in each compartment over the first 24 h.

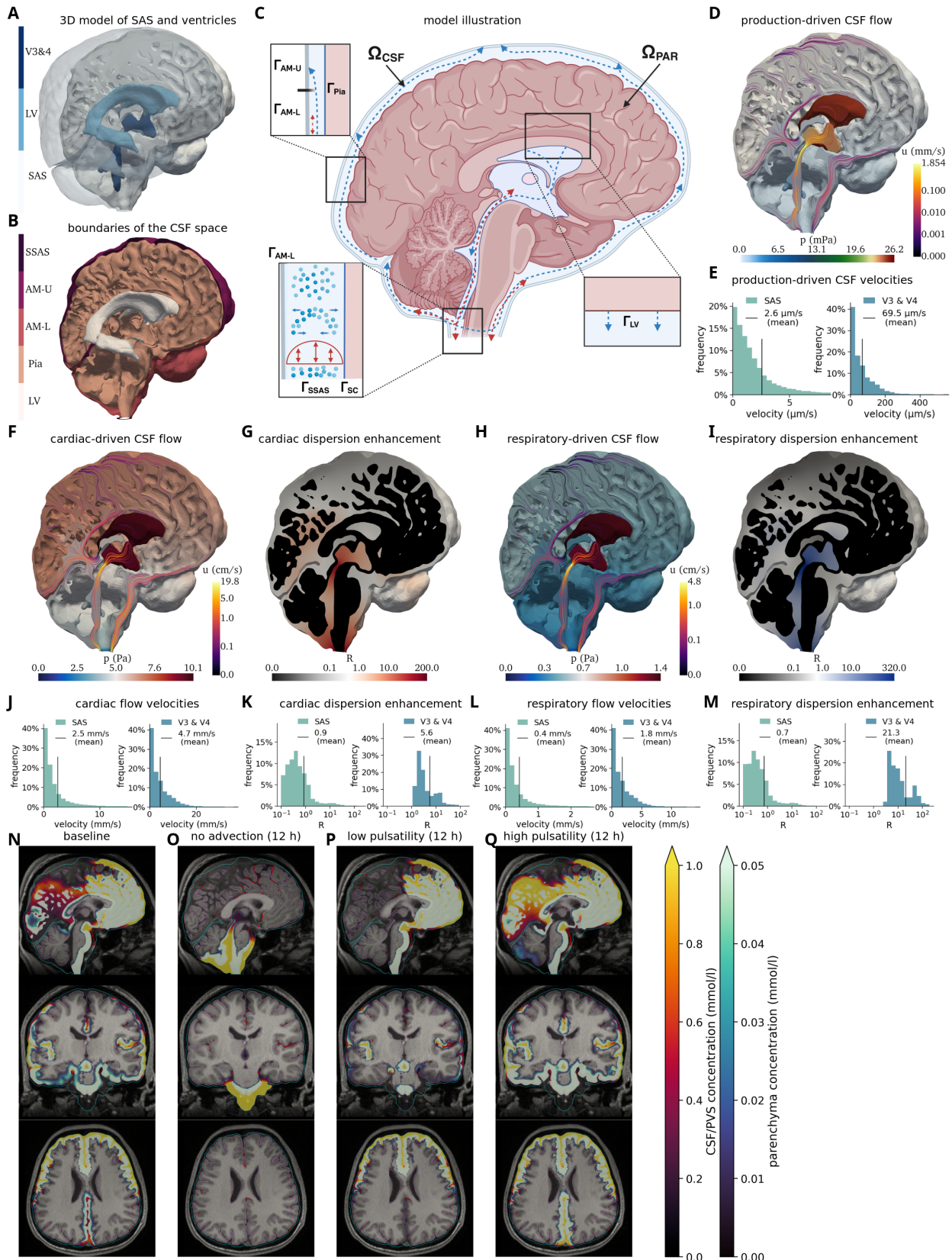


Figure 2. The balance between CSF pulsatility and production shapes tracer enrichment patterns. A) CSF spaces: the third and fourth ventricle (V3&4), lateral ventricles (LV) and SAS; B) Boundaries and interfaces: the spinal subarachnoid space (SSAS), upper and lower arachnoid membrane (AM-U and AM-L), pia (Pia) and lateral ventricles (LV); C) Schematic of the CSF flow model; D) CSF flow induced by CSF production with outflow allowed across the upper convexity (AM-U);

Figure 2. (cont.) E) Histograms of the production-induced CSF velocities in the SAS and third and fourth ventricle (V3 & V4) in terms of the relative frequency of the mean flow speed in each computational cell weighted by its volume; F) CSF flow induced at peak systolic blood inflow; G) Cardiac-induced dispersion factor R_c ; H) CSF flow induced at peak respiratory expansion; I) Respiration-induced dispersion factor R_r , $D = (1 + R_c + R_r)D^{\text{Gad}}$; J–M): Histograms of the cardiac-induced flow velocities (J), cardiac-induced dispersion factors (K), respiratory flow velocities (L), respiratory dispersion factor (M); N–Q): sagittal, coronal and axial planes of tracer concentration after 12h for different model variations: baseline (N), no CSF production (O), low dispersion (P), and high dispersion (Q).

88 easily differ between individuals and between both pathological and physiological states. We therefore next asked to what
 89 extent – and how – variations in CSF pulsatility would affect the intracranial enrichment characteristics.

90 For the CSF dynamics in our baseline model, we combine the net contribution to CSF flow induced by CSF production with
 91 the integrated dispersive effects of cardiac and respiratory pulsatile CSF flow (Figure 2A–C). Beginning with the advective,
 92 net flow field driven by CSF production, we impose a constant CSF inflow of 400 ml/day across the surface of the lateral
 93 ventricles. Simultaneously allowing for efflux across the upper convexity yields a total CSF pressure drop of 26 mPa (0.00020
 94 mmHg) (Figure 2D) with a maximum flow velocity of 1.85 mm/s (in the aqueduct) and a mean velocity in the SAS of 2.6 $\mu\text{m/s}$
 95 (Figure 2E). Next, to examine the dispersive effects of pulsatile CSF flow, we employ the theory of shear-augmented dispersion
 96 together with computational fluid dynamics to determine a dispersion factor R enhancing the effective solute diffusivity (see
 97 Supplementary information S1.3 for a complete description). To estimate the cardiac contribution, we compute the steady state
 98 CSF pressure and flow fields at peak systolic blood inflow. Modelling the reduction in CSF space volume corresponding to
 99 peak systolic conditions, we assume a total inflow rate of 6 ml/s^{57,82} in the SAS across its outer surface and 0.31 ml/s across the
 100 lateral ventricle surface⁵⁶. This scenario sets up a pressure drop of 10 Pa (0.075 mmHg) between the lateral ventricles and the
 101 spinal SAS and a maximum flow velocity of 19.8 cm/s (Figure 2F, J). Assuming a cardiac frequency of 1 Hz, we infer that this
 102 cardiac-induced pulsatile CSF flow increases the effective diffusion by more than two orders of magnitude in the aqueduct and
 103 near the cisterna magna, but has little effect ($R < 1$) in most of the SAS (Figure 2G, K). For the respiratory contribution, we
 104 employ the same methodology, but with a total rate of 1 ml/s⁸³ in the SAS and 0.121 ml/s⁸⁴ in the lateral ventricles, yielding a
 105 respiratory peak flow volume of 1.121 ml/s at the craniocervical junction. While the resulting flow velocities are only about
 106 one fourth of their cardiac-induced counterparts (Figure 2H, L), respiratory dispersive mixing reaches a factor of up to 320 due
 107 the lower respiratory frequency of 0.25 Hz (Figure 2I, M).

108 Now, to examine how CSF pulsatility affects the tracer enrichment patterns, we consider three variations of the baseline: (i)
 109 no CSF production, (ii) reduced pulsatility and thus decreased dispersion, and (iii) higher pulsatility with increased dispersion.
 110 We computed the reduced and increased pulsatility scenarios by halving and doubling the inflow rates associated with both
 111 cardiac and respiratory pulsations, which changed the dispersion factors by 0.25× and 4×, respectively. Note that behaviour
 112 directly reflects the nature of our model: Stokes flow is linear in its inflow boundary conditions, and the diffusion enhancement
 113 factor is quadratic in the predicted pressure gradient. Without CSF production, transport is considerably delayed (Figure 2N, O).
 114 Even after 12 hours, tracer remains in the subtentorial regions around the cerebellum, the brain stem and in the surrounding CSF.
 115 Interestingly, the lack of CSF production instead allows tracer to travel upwards through the ventricular system, reaching the
 116 third ventricle after around 12 hours. On the other hand, if the CSF pulsatility is reduced, we observe rapid transport towards
 117 the upper convexity of the cranium, as in the baseline model, but the tracer spreads exclusively within the anterior regions
 118 (Figure 2P). This feature can be attributed to the CSF flow bifurcation posterior to the ambient cistern (Figure 2D): without
 119 sufficient diffusion, the tracer is unable to cross into the posterior SAS. Indeed, with higher dispersion, the tracer moves through
 120 the quadrigeminal cistern and further upwards into the longitudinal fissure, with also enrichment of the cerebellum (Figure 2Q).

121 Perivascular flow shapes and accelerates molecular transport

122 The PVSs are recognized across species as critical pathways for solute transport in and around the brain, and thus as potential
 123 targets for enhancing brain drug delivery and metabolic waste clearance. However, whether CSF flows more rapidly in PVSs and
 124 what the forces and mechanisms required to drive such flow are, remain as key points of debate^{14,28}. Motivated by experimental
 125 observations in animal models^{10,32–34}, there is now a remarkable body of literature on modelling perivascular fluid flow and
 126 transport^{37–48}. Here, we ask how these proposed mechanisms would translate from idealized geometries to human vascular
 127 networks and moreover, evaluate their integrated effect in the context of intracranial solute transport.

128 Our periarterial network extends from the internal carotid arteries and basilar artery through up to 18 bifurcations to reach
 129 upstream network ends located within the SAS or up to 6 mm inside the parenchyma (Figure 1A–B, Figure 3A) and includes
 130 major surface arteries of radius 0.5–1.4 mm. Due to imaging limitations, the network primarily covers the supratentorial
 131 regions, with the lowest network point located approximately 4 cm above the craniocervical junction. Imposing the pressure
 132 field induced by CSF production at the periarterial network ends induces slow steady CSF flow of variable direction in these

PVSs, with an average velocity of 0.08 $\mu\text{m/s}$ (antegrade) and a maximum velocity of 0.55 $\mu\text{m/s}$ (Figure 3B). On the other hand, traveling waves of arterial wall motion (Figure 3C), such as the pulse wave or other vasomotion^{9,85–88}, also induce net directional flow in the PVS^{40–42,46,89} – of magnitude and direction depending on the amplitude, frequency, and length of the waves and the characteristics of the perivascular network⁴¹. Applying a semi-analytic model of the net flow induced by peristalsis in perivascular networks⁴¹ (see Methods), we estimate that the cardiac pulse wave alone, traveling at a frequency of 1 Hz with a wavelength of 2.0 m and a 1% wall displacement⁹⁰, will induce mainly antegrade PVS flow with an average net velocity of 0.92 $\mu\text{m/s}$ while reaching up to 7.31 $\mu\text{m/s}$ near larger, ventral vessels such as the MCA (Figure 3D,E). The same theory predicts that strong ultraslow vasomotions, if traveling antegrade at 0.1Hz with a wavelength of 0.02 m and a 10% displacement⁸⁸, will induce both retrograde and antegrade net PVS flow with an average velocity of 13.05 $\mu\text{m/s}$ and maximum velocity 54.44 $\mu\text{m/s}$ (Figure 3D,F).

We study the effect of such rapid PVS flow on intracranial molecular transport by comparing the more conservative baseline model and a high PVS flow model, where the former still includes the net flow contributions from CSF production and the cardiac pulse wave, while the latter additionally includes the ultraslow vasomotion contribution. In both models, tracers were first observed at the basal artery after 48 minutes (Figure 4A), defined by their first-time arrival (FTA), the time at which the concentration first exceeds 0.1 mmol/l. At all upstream locations along the middle cerebral arteries (MCAs) and anterior cerebral artery (ACA), we found substantially reduced FTAs with higher PVS flow (Figure 4B), up to 2.5 hours earlier in the left M2 segment of the MCA. PVS concentrations peaked before the surrounding tissue (0:48h vs 1:12h at the MCA and 1:00h vs 1:48h at MCA2) with high PVS flow, while these peaks occurred nearly simultaneously in the baseline model. The earlier appearance and the delay in time-to-peak between the PVS and surrounding tissue clearly indicates the directionality of tracer enrichment – it first arrives in the PVS and subsequently spreads into the tissue and SAS (Figure 4C, D), and especially so with higher PVS flow. These observations also hold on an aggregated level: computing the total amount of tracer in the PVS as a function of the distance to the arterial network roots, we find accelerated tracer transport with higher PVS flow, especially at earlier time points (2–9 hours) (Figure 4E). Moreover, differences in tracer transport along the PVS translate to altered enrichment patterns on the whole-organ scale. For instance, after 4–6 hours, the faster-moving tracer in the PVS is clearly visible in the space adjacent to the PVS of the ACA, MCA, and other arteries (Figure 4G). In contrast, there are no clear signs of early enrichment surrounding the PVS in the baseline model (Figure 4F).

A natural question is whether early PVS enrichment could be the result of increased dispersion rather than net flow in the PVS^{43,44,47,87}. Interestingly, even increasing the dispersion factor by 100× in the PVS, induced only minor changes in the global spreading rate compared to the baseline (Figure 4F, H), thus indicating a negative answer to this question.

Structural versus functional compartmentalization of perivascular spaces

Human and rodent observations indicate that tracers concentrate in perivascular spaces surrounding the pial and subarachnoid vasculature^{23,29,33,34,61,91}. However, it remains unclear whether such enrichment patterns necessitate a structural barrier, such as a membrane with limited permeability, or if the patterns could result from enhanced flow or mixing in these areas alone. We therefore next investigate how the permeability of the interface between the PVS and the surrounding CSF affects tracer enrichment around the major arterial trunks (Figure 5A–B). To this end, we compare models with high and low permeabilities, representing a highly permeable PVS-CSF interface (functional compartmentalization) and a less permeable interface (structural compartmentalization), respectively. For the low permeability model, we set the permeability to $3.8 \cdot 10^{-7} \text{ m/s}$, consistent with previous estimates for the endfoot sheath surrounding penetrating arterioles⁹², which we consider to be a lower bound for the surface PVS-CSF permeability. For the high permeability model, we increase this permeability by a factor of 100. We emphasize that, for both scenarios, we consider the high PVS flow regime as examined in the previous section.

At the basal artery (BA), tracer appears within one hour in the surrounding CSF in both models (Figure 5C, E). With a more permeable PVS-CSF interface, tracer quickly crosses from the CSF into the PVS, resulting in similar peak concentrations of 25 mmol/l in the PVS and at its outer surface, while values up to 50 mmol/l are attained in the vicinity. In contrast, the low permeability model exhibits substantially lower perivascular tracer enrichment, with a maximum concentration of 10 mmol/l after approximately two hours. For the middle cerebral arteries (MCA-R and MCA-L), tracer appears first in the PVS in both models (Figure 5D, E), though with higher concentrations in the high permeability model (up to 24 mmol/l). We also observe that the higher permeability allows the tracer to leak out of the PVS and spread within the Sylvian fissure to a greater extent. With a small delay, more tracer appears via the CSF pathway (Figure 5D). At the anterior cerebral artery (ACA-A2), the first tracer arrival in the PVS occurs after 3 hours, with a peak at 5 hours. The concentration peak in the PVS is tailed by a higher peak in the CSF (Figure 5E), indicating tracer arrival through a second pathway; i.e., directly through the CSF-filled space outside of the PVS. Similar patterns are observed for ACA-A3.

Summarizing and quantifying these observations (Figure 5F), we find that neither the time of first arrival nor the time-to-peak are substantially affected by the PVS-CSF permeability at any of the periarterial segments considered (BA, MCAs, ACAs). However, the concentration difference between the PVS and its surrounding CSF quickly decreases with higher permeability,

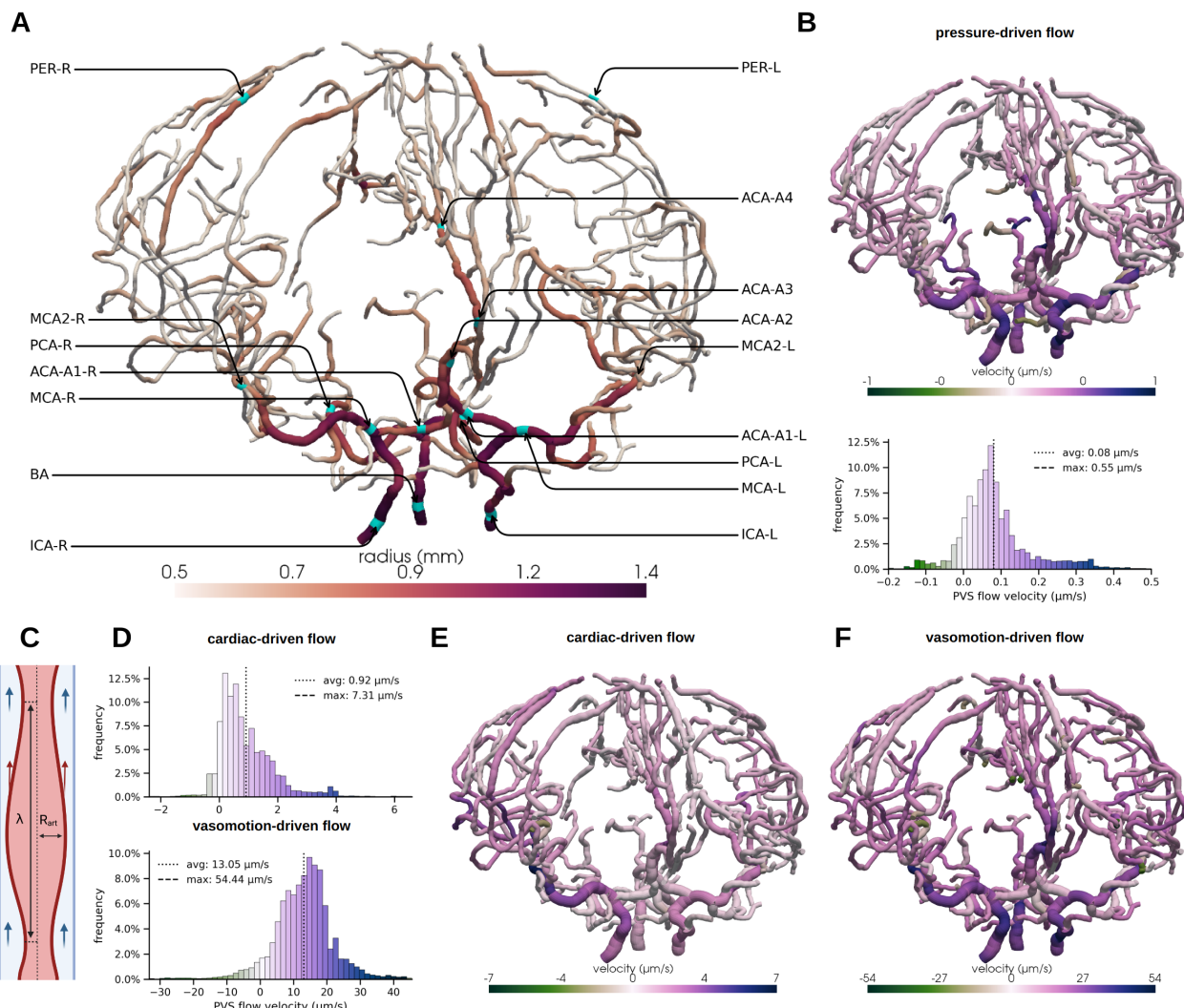


Figure 3. A static pressure gradient and peristaltic pumping are potential drivers of perivascular flow. A) Surface arterial network colored by arterial radius with vessel locations labeled; B) Net PVS flow induced by CSF production alone (see also Figure 2D). Histograms show the relative frequencies of local periarterial velocities. Positive values indicate antegrade PVS flow, while negative values indicate retrograde PVS flow; C) Illustration of the concept of peristaltic pumping; D) histograms of estimated net PVS flow induced by pulse wave or vasomotion peristaltic pumping; E) Estimated net PVS flow induced by pulse wave peristaltic pumping alone. F) Estimated net PVS flow induced by vasomotion/slow wave peristaltic pumping alone.

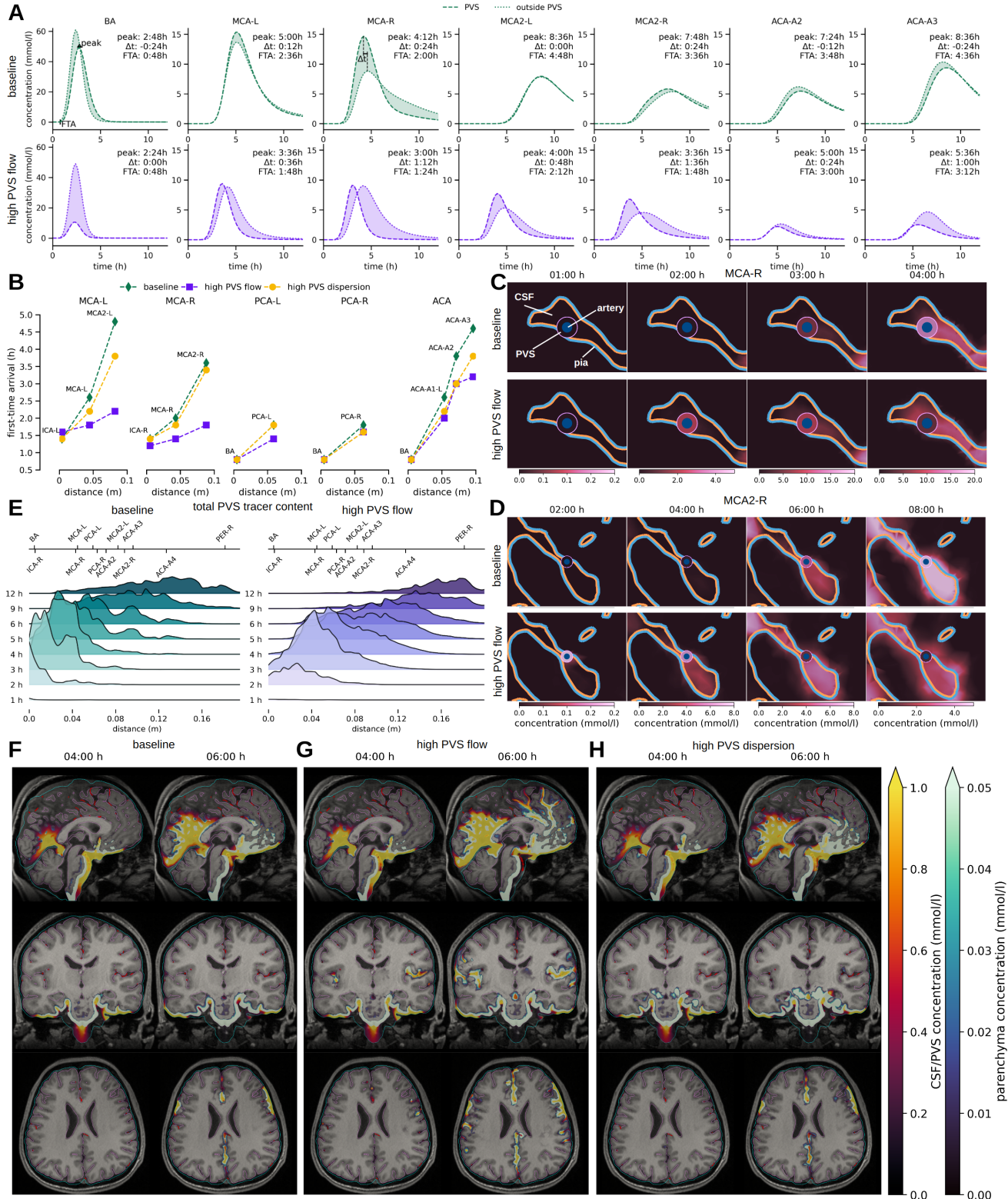


Figure 4. Perivascular flow shapes and accelerates molecular transport. A) Comparison of mean tracer concentration in the PVS and over the outer PVS surface at key locations of the arterial tree, for the baseline (lower) and high PVS flow (upper) models, with labels: “peak”: time-to-peak (h), “ Δt ”: time difference between peaks (h), and “FTA”: first-time tracer arrival (h). B) first-time arrival for the main trunks of the periarterial network over the distance from the closest network root node (BA, ICA-R or ICA-L for the baseline, the high PVS flow and the high PVS dispersion models);

Figure 4. (cont.) C, D) 2D slices showing zoom-in on the region surrounding the MCA-R and MCA2-R for the baseline (upper) and high PVS flow (lower) models. Innermost circle indicates the artery (blue), the surrounding annulus is the PVS (color represents concentration value), the surroundings are parenchyma and/or CSF spaces, separated by the pia (blue: towards the parenchyma, pink: towards the CSF); E) Total amount of tracer in the periarterial spaces as a function of the distance to the nearest network root over time for the baseline (left) and the high PVS flow (right) models; F–H) sagittal (upper) and coronal (lower) views of the simulated tracer concentrations overlayed on the T1-weighted MR image after 4 and 6h for the baseline (K), high PVS flow (L) and high PVS dispersion (M) models (concentration opacity linearly increasing with concentration value, pial surface outlined in pink, arachnoid membrane in cyan, and arteries in dark red). An interactive visualization of the baseline and the high PVS flow model can be found [here](#), and [here](#).

as does the time lag between the concentration peaks in these domains. Thus, fast transport along the PVS is not contingent upon a structural compartmentalization of the PVS, whereas a sharp concentration gradient between PVS and CSF is unlikely without a restricting barrier.

Enlarged PVSs in the SAS delay periarterial and intracranial tracer enrichment

Idiopathic normal pressure hydrocephalus (iNPH), a dementia subtype, is associated with enlarged PVS in the SAS and impaired periarterial and parenchymal tracer transport²⁹. More generally, enlarged PVSs are associated with a range of pathophysiological conditions and cognitive decline⁹³. A key question is thus whether enlarged PVSs alone leads to delayed perivascular and intracranial tracer enrichment. To address this question from a fluid and transport dynamics perspective, we ask our in-silico model to predict the integrated effect of perivascular dilation on PVS flow velocities and tracer enrichment patterns (Figure 6A).

Again we compute CSF production-, cardiac-, and vasomotion-induced net PVS flow velocities, but now in a perivascular geometry with an increased outer radius ($R_2^{\text{dilated}} = 3R_1$) compared to the previous ($R_2^{\text{control}} = 2R_1$), which corresponds to a $2.67 \times$ increase in PVS cross-section area. The enlargement yields notable and non-uniform changes in the flow dynamics. On the one hand, the pressure-induced flow velocities increase from a mean of $0.08 \mu\text{m/s}$ to $0.33 \mu\text{m/s}$ due to the reduced effective resistance of the PVS. However, the peristaltic pumping becomes considerably less effective: the cardiac and vasomotion-induced net CSF flow velocities drop from a mean of $0.92 \mu\text{m/s}$ to $0.17 \mu\text{m/s}$ and from $13.05 \mu\text{m/s}$ to $2.33 \mu\text{m/s}$, respectively (Figure 6B–D). In total, the net CSF velocity reduces, which in turn alters the tracer enrichment within the dilated PVS. Notably, we observe later tracer arrival in all MCA segments, with up to 96 min later arrival in the MCA2s for the high PVS flow scenario (Figure 6E, F). For the baseline model, which omits the vasomotion-induced net PVS flow, the effect is less pronounced in the MCA but clearly persists and is evident in the MCA2s (Figure 6F). Finally, we note that the larger volume of the dilated PVS results in a greater total accumulation of tracer in the PVS from 3–24 hours and reduced enrichment of the parenchyma at 6 and 12 h, while the mean PVS concentration is initially lower, but later exceeds the baseline model (Figure 6G,H).

Discussion

We have presented a high-fidelity in-silico model of molecular transport and clearance in human intracranial spaces, enabling tailored predictions of the influence of CSF space and (peri)vascular morphology, physiological factors such as cardiac and respiratory pulsatility, as well as of pathological conditions such as enlarged PVSs in the SAS. A key observation is that the balance between CSF production and intracranial pulsatility significantly shapes the large-scale features of tracer enrichment, with e.g. ventricular tracer reflux after intrathecal injection in the absence of CSF production, and preference towards anterior brain regions with reduced pulsatility. Indeed, the simulated distribution patterns cover a substantial range of the individual variations observed clinically¹⁵. In terms of perivascular pathways, we find that even moderate CSF flow on the order of $0.1\text{--}1.0 \mu\text{m/s}$ in the surface PVSs results in earlier tracer enrichment around major cerebral arteries. This effect is more pronounced – with up to a three-hour difference in time of arrival – with mean PVS flow rates of approximately $10 \mu\text{m/s}$. Our models of CSF flow in perivascular networks, based on first principles and asymptotic analysis, predict net flow of such magnitudes and both antegrade and retrograde flow within the perivascular network. The PVS may thus function as highways facilitating rapid transport, even in the absence of structural barriers, though a sharp concentration difference between the PVS and surrounding tissues is unlikely without such barriers. Finally, dilated PVS in the SAS will cause a substantial reduction in cardiac- and vasomotion-driven flow velocities, which in turn impedes perivascular transport.

While tracer enrichment of the brain and surrounding CSF spaces have been extensively studied in animal models, especially in murine models in connection with studies of the glymphatic system, there are fewer reports of contrast enrichment in human subjects over 0–24h. We therefore mainly compare our in-silico predictions with the series of papers by Eide and colleagues^{6,11,15,29} and Watts et al⁶⁸. Ringstad et al.¹⁵ report of tracer enrichment in a centripetal pattern, primarily in regions near large cerebral surface arteries, peaking in the CSF spaces between 6 and 9 hours, with parenchymal tracer content still

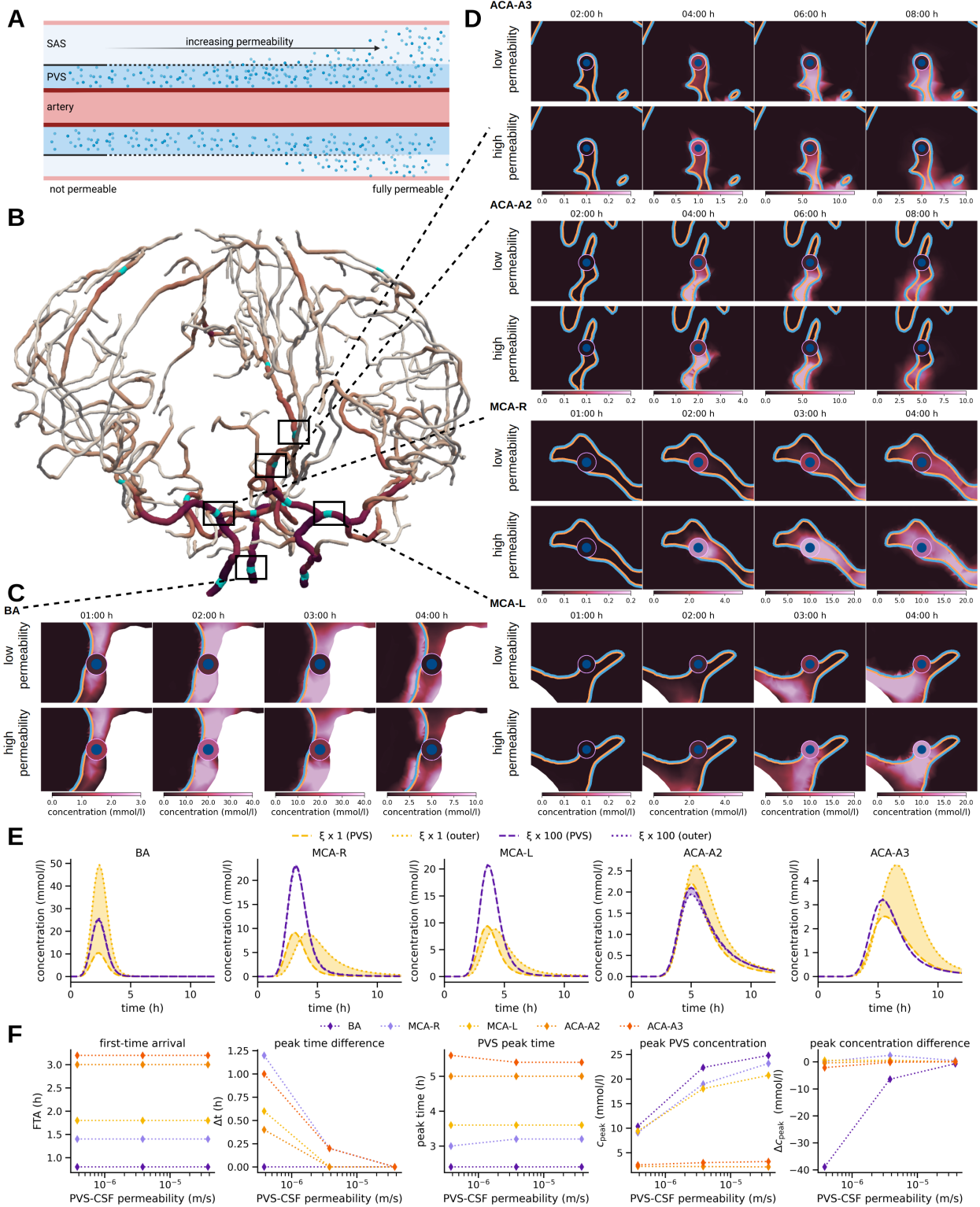


Figure 5. Does early perivascular enrichment rely on a structural compartmentalization of the PVS? A) The PVS-CSF membrane permeability regulates the exchange of solutes between the PVS and surrounding CSF spaces; B) The arterial network with highlighted regions of interest; C) 2D slices showing zoom-in to the region surrounding the basal artery after 1, 2, 3, and 4 hours for a low (above) and high (below) PVS-CSF permeability model. Innermost circle indicates the artery (blue), the surrounding annulus is the PVS (color represents concentration value), the surroundings are parenchyma and/or CSF spaces, separated by the pia (blue: towards the parenchyma, pink: towards the CSF). The cutting planes are normal to the blood vessels; D) As in (C) for regions surrounding (from upper to lower) the ACA-A3, ACA-A2, MCA-R and MCA-L segments;

Figure 5. (cont.) E) Comparison of mean tracer concentration in the PVS (dashed) and over the outer PVS surface (dotted) for the BA, MCA-R, MCA-L, ACA-2, and ACA3 segments over time for the high (purple) and low permeability (yellow) models; F) Effect of varying the PVS-CSF permeability on first-time-of-arrival (FTA), time difference (Δt) between concentration peaks in the PVS and surrounding tissue, time of PVS peak concentration, PVS peak concentration and difference in peak concentration between PVS and surrounding tissue.

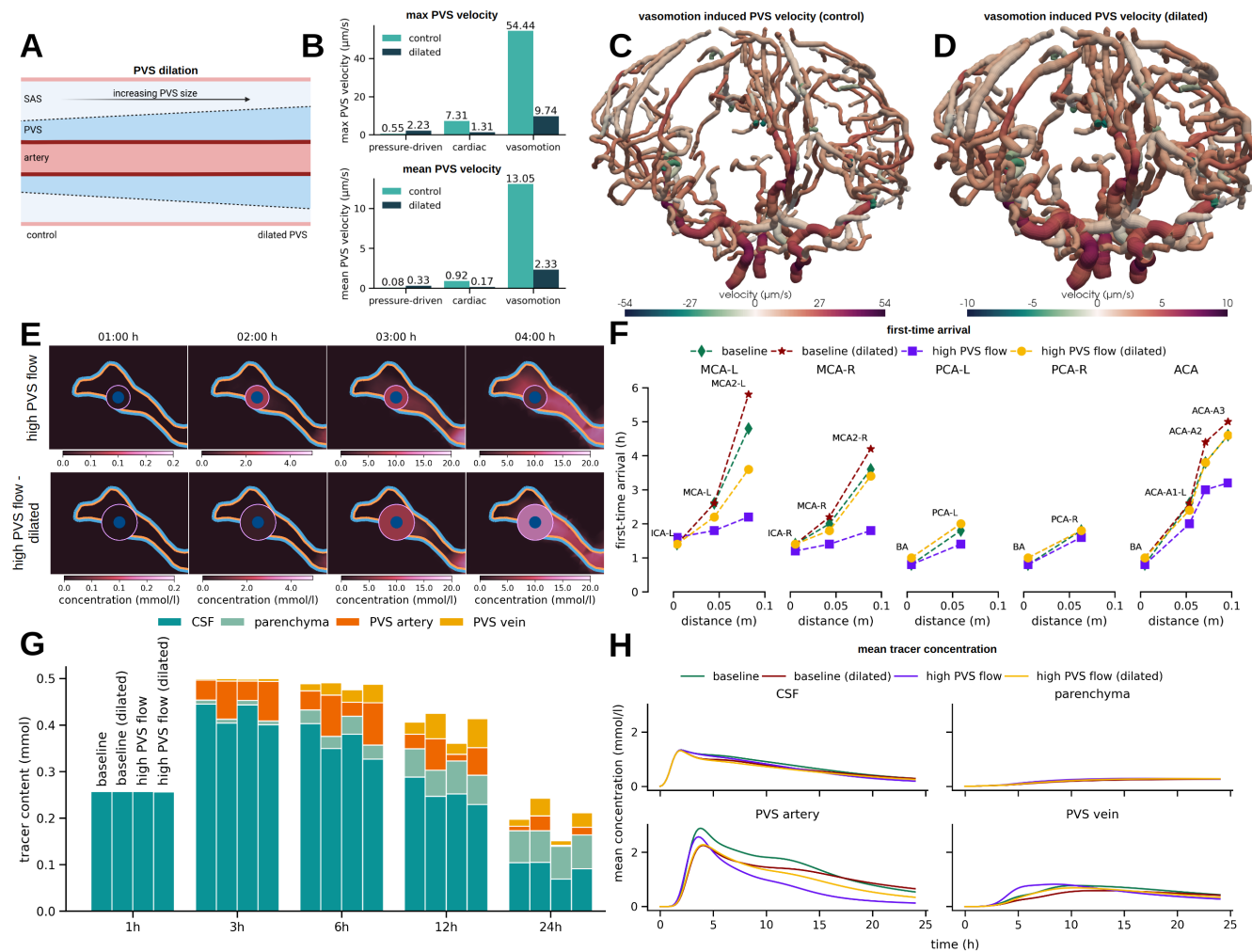


Figure 6. PVS enlargement in the SAS reduces net PVS flow and delays tracer transport A) Modelling dilated PVS in the SAS by extending the outer PVS boundaries; B) mean and max PVS flow velocities with normal/control and dilated PVS; C–D) 3D rendering of vasomotion-induced PVS flow in the normal (C) and dilated (D) periarterial networks; E) 2D slices showing zoom-in to the region surrounding the MCA-R after 1, 2, 3, and 4 h with normal (lower) and dilated (upper) PVS. Innermost circle indicates the artery (blue), the surrounding annulus is the PVS (color represents concentration value), the surroundings are parenchyma and/or CSF spaces, separated by the pia (blue: towards the parenchyma, pink: towards the CSF). The cutting plane is normal to the blood vessel; F) First-time arrival for different branches of the arterial tree for the baseline model (with pressure-driven and cardiac-induced net PVS flow) and the high PVS flow model (also including vasomotion-induced net PVS flow) for normal and dilated PVS; G) total tracer content in the CSF, parenchyma and arterial and venous PVS at 1,3,6,12 and 24 h for the four models from F; H) mean concentration in the CSF, parenchyma and arterial and venous PVS over time for the four models from F.

increasing after 24 hours, but with large individual differences. Watts et al⁶⁸ report of a similar enrichment pattern and a concentration peak in the SAS of ≈ 0.5 mmol/l (relative to a total amount of 1.0 mmol) occurring after 10 to 15 hours. Our in-silico enrichment patterns agree with these observations, though with an earlier rather than later peak in the CSF spaces (2 hours after first tracer appearance at the craniocervical junction). In particular, we note that the substantial individual variation observed clinically is comparable to the variation in in-silico enrichment patterns associated with reduced CSF production or reduced intracranial pulsatility. We find that about 20% of the tracer reaching the cranium enters the parenchyma, which aligns with the reported peak concentration values of 0.5 mmol/l in the SAS and 0.1 mmol/l in the parenchyma reported by Watts et al⁶⁸.

Importantly, our simulation results indicate that the tracer enrichment observed clinically relies on the presence of one or more flow drivers in addition to CSF production and cardiac peristalsis. Dispersion due to cardiac and respiratory pulsations has been hypothesized to enhance transport in the perivascular spaces as well as in the CSF spaces. However, recent estimates indicate that the effect of dispersion in the PVS does not exceed a factor of 2 compared to diffusion alone^{43,44,47,87}. Our model demonstrates that not even a 100-fold increase in the PVS dispersion coefficient accelerates transport substantially (Figure 4H). To illustrate the need for a stronger advective driver, we compared our findings to tracer arrival times reported by Eide and Ringstad²⁹, who observed a delay of just 15.3 min between the M1 and M2 segments of the MCA. First, we note that the spaces studied by Eide and Ringstad²⁹, labeled therein as the PVSAS, are naturally compared to the parts of our surface PVS networks embedded within the SAS. Our baseline model, accounting only for CSF production and cardiac-driven flow, predicted a physiologically unrealistic delay of over three hours. In contrast, our high PVS flow scenario, which incorporates the effects of low-frequency vasomotion, yielded a more consistent delay of 24 minutes. Furthermore, after adjusting for the 13 min travel time from injection to the craniocervical junction²⁹, the high PVS flow model's FTAs (84–108 min for M1) aligns well with the upper end of the reported clinical range (37.8 ± 47.0), particularly when considering potentially delayed transport due to the limited caudal extent of our PVS network. All in all, we interpret these results as strongly indicative of that PVS flow driven by CSF production and cardiac peristalsis alone is insufficient to explain the rapid perivascular transport observed in humans.

The existence, magnitude, and directionality of flow in surface and parenchymal PVSs have been the subject of active debate for decades^{10,14,22,25,31–35,37–42,45,48,85,94}. In mice, Mestre et al³⁴ observe CSF flow in surface perivascular regions surrounding branches of the MCA with average flow speeds of 18.7 $\mu\text{m}/\text{s}$ and net flow in the antegrade direction, but also regions with retrograde flow. Similarly, Bedussi et al.³³ report of oscillatory flow, with an average (net) CSF velocity of 17 ± 2 $\mu\text{m}/\text{s}$ in the antegrade direction. Using physics-informed neural networks, Boster et al³⁵ estimate PVS velocities of 12.75 ± 6.25 $\mu\text{m}/\text{s}$. Less is known about the magnitude and directionality of CSF flow in surface PVSs in humans. Here, assuming that human surface PVS follow the major surface vessels and are CSF-filled but otherwise open regions of width proportional to the vessel radius, our estimates indicate that the CSF pressure differences due to CSF production, cardiac peristaltic pumping and low-frequency vasomotion all yield spatially-varying net CSF flow with both antegrade and retrograde PVS segments. This observation is thus in agreement with the experimental observations^{33,34}, and inherently supports the original notion that antegrade and retrograde solute transport along PVSs may coexist²². In terms of magnitude, the contribution from CSF production and cardiac wall motion are small (0.08 $\mu\text{m}/\text{s}$ and 0.92 $\mu\text{m}/\text{s}$ on average), but intriguingly, our estimates of the contribution from vasomotion (13.05 $\mu\text{m}/\text{s}$) are comparable to the experimental reports. We do note that this estimate is based on the presence of rhythmic waves of vasomotion at a frequency of 0.1Hz, a wavelength of 20 mm, and a wall displacement of 10% – in the antegrade direction, all values currently associated with major uncertainty^{85,86,88,95}. In particular, Broggini et al⁸⁸ report of near-0.1Hz vasomotion waves traveling both antegrade and retrograde along pial arterioles in mice, while Munting et al⁸⁶ report of vessel diameter changes at similar frequencies mainly (but not entirely) in the retrograde direction. To the best of our knowledge, less is known about vasomotion wave characteristics in the human cerebral vasculature, though Gokina et al⁹⁵ report of spontaneous vasomotion also in human pial arteries ex-vivo.

To what extent are surface PVSs in communication with the surrounding SAS and to what extent are these structurally separated compartments? Originally, Weller and coauthors^{23,60,91} identified thin sheaths of pial cells surrounding human surface arteries and penetrating arterioles (but not veins or venules). On the other hand, Bakker and coauthors report that the subarachnoid space, the cisterns, ventricles and penetrating periarteriolar spaces form a continuous CSF space⁶¹. Thorne and colleagues study the architectures of rat perivascular spaces in detail, emphasizing the presence of openings (stomata) on the interface between the vasculature and the CSF within the SAS^{27,62}. Further, Mestre et al⁶³ study the properties of pial perivascular spaces in mice, and report of pial cells forming sheaths for larger surface arteries and partially cover smaller surface arteries, with higher coverage in ventral SAS regions. Our results demonstrate that the PVSs may act as rapid transport pathways even with only a partial barrier between the PVS and surrounding CSF, thus contributing to quantifying the properties of the human PVS-CSF interface²⁹. In this regard, we emphasize that we report on the isolated effect of variations in permeability on molecular transport, separated from any effects on fluid flow in the PVS. Clearly, one may expect that the presence and/or properties of such a barrier would affect also PVS flow. However, considering the uncertainty associated with PVS flow

characteristics in the human SAS in general and the lack of computational models describing net PVS flow in the presence of fluid exchange, this remains challenging to quantify.

Lifestyle factors such as sleep^{5,6,8,9,87,96,97}, exercise^{98,99}, and alcohol intake¹⁰⁰ affect molecular transport and clearance of the brain. In particular, pial arteries display higher-amplitude low-frequency vasomotion during NREM and intermediate sleep states, while REM sleep is associated with reduced PVS width⁸⁷. Peristaltic pumping is more effective under both of these configurations, resulting in higher estimated net PVS flow velocities⁴¹. Even higher PVS velocities would amplify the PVS flow effects simulated here, with earlier arrival times along the PVSs, clear enrichment in adjacent spaces, and accelerated tracer enrichment overall. Moreover, sleep is linked with low-frequency oscillations in human CSF flow⁵⁵. As we have shown here, the level of dispersion in the CSF spaces strongly shapes molecular transport patterns. While we, at baseline, account for the dispersion induced by cardiac and respiratory pulsatility, the high dispersion scenarios considered can be viewed as representative of additional pulsatility induced by e.g. neural waves^{55,58} or other respiration patterns depending on activity level. More broadly, we consider this as a key strength of the current in-silico framework: allowing for integrating and exploring the mechanistic macroscale implications of changes in pulsatility at smaller spatial or temporal scales. This approach of modeling pulsatility through an effective dispersion factor is a simplification that does not capture the full complexity of transient fluid dynamics, such as non-uniform wall motion and ependymal cilia within the ventricular system¹⁰¹, dynamic CSF flow at the craniocervical junction, or the effect of microanatomical features such as subarachnoid trabeculae on flow resistance and dispersion in the SAS. However, our approach is supported by recent clinical observations. High-resolution MRI measurements by Hirschler et al.³⁶ revealed that CSF mobility in regions with high pulsatility is approximately tenfold greater than the self-diffusion of water, an enhancement factor consistent with the values computed in our model.

In terms of limitations, our primary constraint modelling-wise is the geometric representation of the vascular (and therefore also perivascular) networks. Concretely, we account for no vessels below the original MRI resolution limits, and thus only a part of the cerebral surface vasculature and effectively not the cortical vessels. In addition, and again due to lack of resolution, there is uncertainty associated with the location of the vessel segments relative to the CSF spaces and parenchyma, with some vessels surrounded by both domains and some vessels completely entering the parenchyma before returning to the SAS. Higher resolution MRI data (T1w and e.g. time-of-flight, QSM or other modalities) in more subjects would immediately allow for more detailed studies of this aspect. As a result of the lack of an accurate representation of the cortical and subcortical white matter vasculature, we have considered a basic transport model within the parenchyma, modelling extracellular diffusion alone and no bulk interstitial fluid flow. To compensate, we have focused on reporting detailed predictions in the CSF spaces and surface PVS after not more than 24 hours. In particular, we note that, we observe tracer accumulation at the perivascular network ends after 12 hours, similar to that previously observed for microspheres^{33,34}, which here can be interpreted as an artifact of the incomplete network creating a barrier for tracer movement. Previously, by inferring transport parameters within the human brain from glymphatic MRI data, we have found that molecular transport within the parenchyma is well-represented by $\approx 3\times$ enhanced diffusion augmented by local clearance e.g. across the blood-brain barrier, or by diffusion-convection with a complex pattern of spatially-varying interstitial fluid flow on the order of 1-10 $\mu\text{m}/\text{min}$ ⁹⁶. We will incorporate such transport mechanisms within the parenchyma in future work. Finally, we also note that we simulate the intracranial distribution of a tracer concentration appearing at the craniocervical junction rather than as an intrathecal injection. We thus neglect absorption of both CSF and tracer in the spinal compartment, and therefore overestimate the amount of tracer entering into the intracranial spaces; however, due to the linearity of the mathematical model, it is valid to directly interpret the in-silico concentrations relative to the total amount of tracer.

In conclusion, our findings transfer insights from experimental studies and theoretical analysis to the in-silico human setting, reconcile seemingly conflicting observations in particular relating to directionality of perivascular flow, and integrate different physical mechanisms across spatial and temporal scales. The complete simulation pipeline is openly available, including interactive visualization of simulation results for all model variations⁶⁹. Future work will focus on further model validation including comparisons between in-silico predictions and glymphatic MRI for a number of subjects across several patient cohorts. Looking ahead, this platform establishes a foundation for in-silico studies of molecular movement within the human brain environment, such as tailored predictions of intrathecal chemotherapy delivery or personalized diagnostics of brain clearance capacity.

Methods

This section gives a condensed summary of the in-silico modelling framework. For a complete description of the mathematical models and simulation scenarios, we refer to the Supplementary information S1.

Intracranial compartments: ventricular system, SAS, and brain parenchyma

From T1-weighted MR images of a 26-year-old, healthy male volunteer⁶⁷, we first automatically segment the brain parenchyma and CSF spaces, including the ventricular system and SAS, using Synthseg^{102,103} (Figure 1A–B). We next manually adjust the

segmentation to accurately represent the connections and barriers between CSF spaces (aqueduct, median aperture, tentorium cerebelli), smoothen, and finally extract surface representations of the outer (arachnoid) boundary, the pial membrane and other interfaces. Conforming to these surface and interface representations, we generate a tetrahedral mesh Ω representing the complete intracranial volume as the union of the parenchyma Ω_{PAR} and CSF spaces Ω_{CSF} , using fTetWild¹⁰⁴ (Figure 2A–B). The resulting computational mesh consists of 233 592 vertices and 1 290 131 mesh cells, which vary between 0.22 mm and 8.9 mm in mesh cell diameter. The parenchyma has a total volume of 1318 ml, whereas the ventricles and the outer SAS contribute 32 ml and 329 ml, respectively, to a total CSF volume of 361ml, in agreement with recent estimates¹⁰⁵.

Periarterial and perivenous spaces

To represent surface networks of periarterial and perivenous spaces, we use Kiminaro¹⁰⁶ to separately skeletonize time-of-flight angiography (ToF) and quantitative susceptibility mapping (QSM) images from the same human subject⁶⁷. This technique yields networks of one-dimensional curves, each curve Λ^i indicating the centerline of a blood vessel segment and labeled with its lumen radius R_1^i (Figure 3A). We also assign an outer radius $R_2^i > R_1^i$ to each segment i , form the annular cylinder ensheathing Λ^i and define the union of these as the PVS. The periarterial network graph consists of 12 708 edges connected at 12 562 inner nodes and with 147 end nodes, and the associated domain is denoted by Λ_a . We identify three of the end nodes – corresponding to the two internal carotid arteries (ICAs) and the basilar artery (BA) – as root nodes, and designate the other ends as leaf nodes. The resulting perivenous network graph consists of 24 829 edges connected at 23 881 inner nodes and with 949 end nodes, and the associated domain is denoted by Λ_v . Finally, we label the outer surface of the PVSs associated with Λ_a and Λ_v , by Γ_a and Γ_v respectively.

Steady flow in the CSF spaces induced by CSF production

We model CSF as an incompressible Newtonian fluid at low Reynolds and Womersley numbers via the Stokes equations with viscosity μ (see Table 1 for parameter values). To account for steady flow induced by CSF production, we compute the CSF velocity field \mathbf{u}_{CSF} and associated pressure field p_{CSF} in the SAS and ventricular system Ω_{CSF} that result from a steady CSF production at a rate of u_{in} across the lateral ventricle walls (Figure 2A–E). We allow for CSF efflux across the upper, outer (arachnoid) boundary with efflux resistance $R_{\text{CSF},0}$.

Perivascular fluid flow induced by CSF production

To estimate the contribution also to perivascular fluid flow from CSF production, we impose the fluid pressure p_{CSF} induced by CSF production, computed in the SAS and ventricular system, at the end nodes of the periarterial network. For the end nodes located within the SAS ($v \in \Omega_{\text{CSF}}$), the value $p_{\text{CSF}}(v)$ is used directly, while for the end nodes located within the parenchyma ($v \in \Omega_{\text{PAR}}$), we compute and apply a harmonic extension $E(p_{\text{CSF}})(v)$. We then numerically solve a system of hydraulic network equations to compute \hat{u}_a^P defined over Λ_a ; i.e., the CSF production-induced velocity field in the periarterial network. We refer to Supplementary information S1.1.4 *Steady flow in perivascular networks induced by pressure differences* for details. We repeat this procedure to compute a corresponding velocity field \hat{u}_v^P in the perivenous network Λ_v .

Dispersion in the CSF spaces induced by pulsatile CSF flow

The pulsatile flow of CSF in the SAS and ventricular system, associated with the cardiac and respiratory cycles, substantially enhances molecular diffusion through dispersion^{43, 44, 47, 78, 107, 108}. To account for these dispersive effects, while bridging from the pulsatile flow time scale of seconds to a molecular transport time scale of hours, we estimate cardiac- and respiratory dispersion factors (R_c and R_r) in Ω_{CSF} (Figure 2G, I). To compute these spatially-varying factors, we rely on a simplified model that combines computational estimates of peak CSF pressure gradients (Figure 2F, H) with theoretical estimates for shear-augmented (Taylor) dispersion^{44, 107, 108} (see Supplementary information S1.3 *Estimating dispersion factors from pulsatile CSF flow* for a complete description). Combining the cardiac and respiratory effects, we set $R = R_c + R_r$ in Ω_{CSF} .

Perivascular fluid flow induced by arterial wall motion

Using the theoretical framework introduced by Gjerde et al.⁴¹, we also compute analytic estimates for the time-average perivascular flow rate $\langle Q' \rangle$ induced by peristalsis in the arterial network Λ_a ; i.e. the net flow induced by traveling waves of arterial wall motion of frequency f , amplitude ϵ and wave lengths λ (Figure 3C). The corresponding contribution to the periarterial flow velocity is defined for each segment Λ_i as $\langle Q'_i \rangle / A_i$ where $A_i = \pi(R_2^i - R_1^i)$ is the cross-section area of the PVS segment and $\langle Q'_i \rangle$ is the estimated mean flow rate (see Supplementary information S1.4 *Estimating net perivascular flow induced by peristaltic waves* for more details). Two wall motion patterns are considered: *cardiac* pulsations with $f = 1.0\text{Hz}$, $\lambda = 2\text{ m}$ and $\epsilon = 1\%$ yielding \hat{u}_a^c (Figure 3D), and very low-frequency *vasomotion* with $f = 0.1\text{Hz}$, $\lambda = 0.02\text{m}$, and $\epsilon = 10\%$ yielding \hat{u}_a^v (Figure 3E). No flow induced by peristalsis is considered for the perivenous network. In the baseline model, we combine the contributions from CSF production and cardiac peristalsis to set \hat{u} as $\hat{u}_a = \hat{u}_a^P + \hat{u}_a^c$ in Λ_a , and $\hat{u}_v = \hat{u}_v^P$ in Λ_v . We

386 remark that none of these models account for fluid exchange across the lateral outer interface of the PVSs (over Γ_a, Γ_v), while
 387 fluid entry and exit is allowed at the end nodes of the PVS networks.

388 Molecular transport equations

We represent the evolution and distribution of a solute in the CSF spaces Ω_{CSF} , brain parenchyma Ω_{PAR} , and periarterial and perivenous networks $\Lambda_a \cup \Lambda_v$ via a mixed-dimensional transport model⁶⁶ over a timescale of minutes to hours (Figure 1A–B, Figure 2A–C). The current model accounts for solute exchange between the CSF spaces, brain parenchyma, and the PVSs, diffusion within all compartments, dispersion and convection in the CSF spaces, and convection within the PVS. Specifically, for $t > 0$, we solve for a concentration field $c(x, t)$ in the 3D intracranial compartments (for $x \in \Omega_{\text{CSF}} \cup \Omega_{\text{PAR}}$) and for a cross section-averaged concentration field $\hat{c}(s, t)$ in the perivascular networks (for $s \in \Lambda_a, \Lambda_v$) satisfying the following equations:

$$\partial_t c - \nabla \cdot D(1+R)\nabla c + \nabla \cdot (\mathbf{u}_{\text{CSF}c}) + \xi(\bar{c} - \hat{c})\delta_\Gamma = 0 \quad \text{in } \Omega_{\text{CSF}}, \quad (1a)$$

$$\partial_t(\phi c) - \nabla \cdot D^*\nabla(\phi c) + \nabla \cdot (\mathbf{u}_{\text{PAR}c}) + \xi(\bar{c} - \hat{c})\delta_\Gamma = 0 \quad \text{in } \Omega_{\text{PAR}}, \quad (1b)$$

$$\partial_t(A\hat{c}) - \partial_s(\hat{D}A\partial_s(\hat{c})) + \partial_s(A\hat{u}\hat{c}) + \xi P(\hat{c} - \bar{c}) = 0 \quad \text{in } \Lambda_a, \Lambda_v. \quad (1c)$$

389 In (1a), D is the (free) diffusion coefficient of the solute, R is the dispersion coefficient in the CSF spaces, \mathbf{u}_{CSF} is the steady
 390 CSF velocity, ξ is a permeability allowing for transfer/exchange across the interfaces Γ_a, Γ_v between the periarterial and
 391 perivenous networks and their surroundings, the overlined \bar{c} denotes the average of c over cross-sections of Γ_a, Γ_v , and δ_Γ
 392 is a Dirac term concentrated on Γ_a, Γ_v . Additionally, in (1b), $\phi = \phi_{\text{ECS}}$ is the brain extracellular volume fraction, D^* is the
 393 effective diffusion coefficient in the parenchyma, and \mathbf{u}_{PAR} is an interstitial fluid velocity. In this study, we set $\mathbf{u}_{\text{PAR}} = 0$. In (1c),
 394 $A = \pi(R_2^2 - R_1^2)$ is the area and $P = 2\pi R_2$ is the perimeter of the PVS cross-sections, \hat{D} is the effective diffusion coefficient in the
 395 PVSs, and \hat{u} is the fluid velocity (in the axial direction) in the PVS defined for the periarterial and perivenous spaces separately
 396 ($\hat{u}|_{\Lambda_a} = \hat{u}_a, \hat{u}|_{\Lambda_v} = \hat{u}_v$). Further, we model the membrane between the parenchyma and the CSF spaces as a semi-permeable
 397 membrane with permeability coefficient β_{pia} , allowing for a jump in c there. The initial concentrations in Ω and networks
 398 Λ_a, Λ_v are all set to zero.

399 Molecular clearance from the intracranial space and perivascular network ends

400 We model molecular clearance, into the meningeal lymphatics or other pathways, across the upper, outer (arachnoid) boundary
 401 (Figure 1A, Figure 2C), proportional to the concentration in the SAS with a rate constant β_{exit} . We set a no-flux condition at the
 402 end nodes of the perivascular networks, not allowing for direct molecular clearance there.

403 Intracranial influx after intrathecal injection

To represent molecular influx into the intracranial compartments following intrathecal injection, without modelling the spinal compartment explicitly, we prescribe a time-dependent molecular influx over the interface towards the spinal CSF compartment with the condition

$$(D\nabla c - \mathbf{u}_{\text{CSF}c}) \cdot \mathbf{n} = g_{\text{influx}}, \quad \text{on } \Gamma_{\text{SSAS}}.$$

Here we set

$$g_{\text{influx}}(t) = \frac{m_{\text{tot}}}{T_{\text{max}}^2 |\Gamma_{\text{SSAS}}|} \max(0, T_{\text{max}} - |t - T_{\text{max}}|), \quad (2)$$

404 which expresses a hat-shaped influx function with a peak at T_{max} and a total tracer injection of m_{tot} (Table 1). We here consider
 405 a fixed $T_{\text{max}} = 1.0$ h in (2), and do not consider the effect of e.g. reduced pulsatility on spinal transit time.

406 Model and material parameters

407 Model and material parameters are summarized in Table 1, and Table 2 gives an overview of the different in-silico scenarios.
 408 The effective diffusion coefficient is set equal to that of Gadobutrol in water in the PVS networks $\hat{D} = D \equiv D^{\text{Gad}}$; is weighted
 409 by the dispersion factor R in the CSF spaces: $(1+R)D$; and modulated by the porosity and tortuosity ($\lambda = 1.78$) in the
 410 parenchyma $D^* = D_{\text{PAR}}^{\text{Gad}}$. We set ξ depending on whether the PVS segment is fully embedded within the CSF spaces ($\xi = \xi_{\text{PVS}}$)
 411 or parenchyma ($\xi = \xi_{\text{EF}}$), or neither (see also Supplementary information S1). To account for the unresolved continuation of the
 412 perivascular network beyond the imaging resolution limit, we implemented a permeability gradient to avoid artificial tracer
 413 buildup. At the terminal leaf nodes of Λ_a , permeability was increased by a factor of 100 to simulate tracer exchange with the
 414 surrounding CSF/tissue, and linearly decreasing to the baseline value at the adjacent network node.

Parameter	Symbol	Value	Unit	Reference
Extracellular space volume fraction	ϕ_{ECS}	0.2	–	109
Free diffusion coefficient, Gadobutrol	D^{Gad}	$3.8 \cdot 10^{-4}$	mm^2/s	110
Parenchymal diffusion coefficient, Gadobutrol	$D_{\text{PAR}}^{\text{Gad}}$	$1.2 \cdot 10^{-4}$	mm^2/s	79
Permeability coefficient, endfoot sheath	ξ_{EF}	$3.8 \cdot 10^{-7}$	m/s	92
Permeability coefficient, PVS-CSF	ξ_{PVS}	$3.8 \cdot 10^{-7}$	m/s	92
Permeability coefficient, pia	β_{pia}	$2.6 \cdot 10^{-8}$	m/s	111
Molecular efflux rate	β_{exit}	$8.0 \cdot 10^{-7}$	m/s	*
Total amount of injected tracer	m_{tot}	0.5	mmol	29
Molecular influx, time-to-peak	T_{max}	1	h	*
CSF production rate	u_{in}	0.4	1 / day	112
CSF viscosity	μ	0.7	$\text{mPa}\cdot\text{s}$	113
CSF outflow resistance	$R_{\text{CSF},0}$	10^4	$\text{Pa}\cdot\text{s}/\text{m}$	*
Dispersion factor, CSF spaces	R	†	–	*

Table 1. Model parameters. †/* denotes computed/estimated within this work. The diffusion coefficient D^{Gad} represent the diffusion coefficient of Gadobutrol in CSF (water), and $D_{\text{PAR}}^{\text{Gad}}$ its effective diffusion coefficient in human cortical tissue, both at body temperature 77,79,110. We use the astrocytic endfeet permeability ξ_{EF} estimated by Koch et al. 92, and we set $\xi_{\text{PVS}} = \xi_{\text{EF}}$ as a baseline.

No.	Model description	\mathbf{u}_{CSF}	$\hat{u} _{\Lambda_a}$	$\hat{u} _{\Lambda_v}$	R	ξ_{PVS}	R_2
0	baseline	\mathbf{u}_{CSF}	$\hat{u}_a^p + \hat{u}_a^c$	\hat{u}_v^p	$R_c + R_r$	ξ_{EF}	$2R_1$
1	no CSF production	0	\hat{u}_a^c	0	$R_c + R_r$	ξ_{EF}	$2R_1$
2	reduced CSF pulsatility	\mathbf{u}_{CSF}	$\hat{u}_a^p + \hat{u}_a^c$	\hat{u}_v^p	$R_c^{\text{red}} + R_r^{\text{red}}$	ξ_{EF}	$2R_1$
3	increased CSF pulsatility	\mathbf{u}_{CSF}	$\hat{u}_a^p + \hat{u}_a^c$	\hat{u}_v^p	$R_c^{\text{inc}} + R_r^{\text{inc}}$	ξ_{EF}	$2R_1$
4	higher PVS flow	\mathbf{u}_{CSF}	$\hat{u}_a^p + \hat{u}_a^c + \hat{u}_a^v$	\hat{u}_v^p	$R_c + R_r$	ξ_{EF}	$2R_1$
5	higher PVS exchange	\mathbf{u}_{CSF}	$\hat{u}_a^p + \hat{u}_a^c + \hat{u}_a^v$	\hat{u}_v^p	$R_c + R_r$	$100 \xi_{\text{EF}}$	$2R_1$
6	dilated PVS in the SAS	\mathbf{u}_{CSF}	$\tilde{u}_a^p + \tilde{u}_a^c + \tilde{u}_a^v$	\tilde{u}_v^p	$R_c + R_r$	ξ_{EF}	$3R_1$

Table 2. Overview of model variations, with color highlighting changes from the baseline model. \mathbf{u}_{CSF} is the CSF velocity field induced by CSF production in Ω_{CSF} , and \hat{u}_a^p and \hat{u}_v^p are the axial velocities induced in the periarterial and perivenous networks, respectively, by the corresponding CSF pressure p_{CSF} . Moreover, \hat{u}_a^c and \hat{u}_a^v are the periarterial velocities induced by arterial pulse wave wall motion and slow vasomotion, respectively. In the model variation with no CSF production, $\mathbf{u}_{\text{CSF}} = 0$, $p_{\text{CSF}} = 0$, and thus $\hat{u}_a^p = \hat{u}_v^p = 0$. $R_c + R_r$ is the combined cardiac and respiratory dispersion factor in the CSF spaces, with model variations $R_{r/c}^{\text{red}}$ and $R_{r/c}^{\text{inc}}$ corresponding to reduced pulsatility and increased pulsatility, respectively. Each PVS cross-section is modelled as a concentric annulus with inner radius R_1 and outer radius $R_2 > R_1$. Finally, \tilde{u}_a^p , \tilde{u}_v^p , \tilde{u}_a^c and \tilde{u}_a^v are as \hat{u}_a^p , \hat{u}_v^p , \hat{u}_a^c and \hat{u}_a^v , respectively, but with a dilated PVS ($R_2 = 3R_1$).

415 Numerical approximation, implementation, and verification

416 We give a concise summary of the numerical approach here (see Supplementary methods for a comprehensive description). To
417 solve (1) numerically, we use the interior penalty discontinuous Galerkin (DG) method with weighted averages and upwinding
418 for the convection term in the 3D domains¹¹⁴ – to ensure numerical stability and minimize the artificial presence of negative
419 concentration values. For the 1D domain, we use continuous finite element spaces defined over each of the networks and
420 stabilized with numerical diffusion when \hat{u} is non-zero. Note that the 3D–1D coupling in (1) leads to a 3D solution c with low
421 regularity properties. Thus, one can only expect lower-order error convergence near Λ_a and Λ_v , see the references¹¹⁵ and¹¹⁶
422 for the numerical analysis of DG and continuous Galerkin schemes, respectively. However, away from these 1D networks,
423 almost optimal approximation is expected^{117,118}. To numerically solve the Stokes equations to compute the CSF flow velocity
424 and pressure in the ventricular system and SAS, we use finite element spaces that preserve the incompressibility condition
425 on the discrete level¹¹⁹. This requirement is important for numerical stability when subsequently solving (1)¹²⁰. The spaces
426 we used for the velocity are continuous along the normal direction; continuity of the tangential component is enforced via
427 interior penalty approaches¹¹⁹. Optimal approximation properties are expected for this scheme. These numerical methods were
428 implemented using the FEniCS finite element framework⁸⁰, and the 3D-1D coupling is handled by the extension FEniCSii⁸¹.
429 The correctness and accuracy of the numerical solutions were verified by a series of numerical verification experiments (see
430 Supplementary information S1.5).

431 The majority of the simulation time was spent on the Stokes flow and transport model simulations. Each Stokes flow
432 simulation utilizes a hybrid parallel approach with 16 MPI processes and 4 threads each, requiring approximately 300 GB of
433 RAM and completing in 23 minutes. The transport model is limited to serial execution by FEniCSii, but employs 16 threads for
434 the linear system factorization, taking 22 minutes and consuming about 50 GB of memory on a AMD EPYC 9684X machine.

435 Comparison with literature results

436 As the primary means of model validation, we compare the in-silico predictions of tracer enrichment and clearance against
437 glymphatic MRI studies (Discussion). In addition, we compare auxiliary model quantities (CSF flow rates and pressure
438 differences, dispersion factor estimates, and the shapes and sizes of PVSs) with the current literature (see Supplementary
439 information S2.1).

440 Data availability

441 Numerical simulation results generated as part of this study are openly available on Zenodo with the identifier doi: 10.5281/zeno-
442 do.14749163. This archive includes surface triangulations used for geometry representation, computational meshes (3D
443 meshes and 1D networks), segmentations, sample simulation outputs from the baseline and high PVS flow models, and
444 animations.

445 Code availability

446 The software developed to generate and analyze the numerical results of this study is openly available on Zenodo with the
447 identifier doi: 10.5281/zenodo.14749163. In addition to simulation and analysis software, this archive also includes surface
448 triangulations used for geometry representation, computational meshes (3D meshes and 1D networks), segmentations, sample
449 simulation outputs from the baseline and high PVS flow models, and animations.

450 References

- 451 1. Rasmussen, M. K., Mestre, H. & Nedergaard, M. The glymphatic pathway in neurological disorders. *The Lancet Neurol.* **17**, 1016–1024 (2018).
- 452 2. Harrison, I. F. *et al.* Impaired glymphatic function and clearance of tau in an Alzheimer’s disease model. *Brain* **143**, 2576–2593 (2020).
- 453 3. Eide, P. K. *et al.* Plasma neurodegeneration biomarker concentrations associate with glymphatic and meningeal lymphatic
456 measures in neurological disorders. *Nat. communications* **14**, 2084 (2023).
- 457 4. Liu, H. *et al.* Glymphatic influx and clearance are perturbed in Huntington’s disease. *JCI Insight* **9** (2024).
- 458 5. Xie, L. *et al.* Sleep drives metabolite clearance from the adult brain. *Science* **342**, 373–377 (2013).
- 459 6. Eide, P. K., Vinje, V., Pripp, A. H., Mardal, K.-A. & Ringstad, G. Sleep deprivation impairs molecular clearance from the
460 human brain. *Brain* **144**, 863–874 (2021).
- 461 7. Eide, P. K. *et al.* Altered glymphatic enhancement of cerebrospinal fluid tracer in individuals with chronic poor sleep
462 quality. *J. Cereb. Blood Flow & Metab.* **42**, 1676–1692 (2022).

- 463 8. Miao, A. *et al.* Brain clearance is reduced during sleep and anesthesia. *Nat. Neurosci.* 1–5 (2024).
- 464 9. Hauglund, N. L. *et al.* Norepinephrine-mediated slow vasomotion drives glymphatic clearance during sleep. *Cell* **0** (2025).
- 465 10. Iliff, J. J. *et al.* A paravascular pathway facilitates CSF flow through the brain parenchyma and the clearance of interstitial solutes, including amyloid-beta. *Sci. Transl. Med.* **4**, 147ra111 (2012).
- 466 11. Ringstad, G., Vatnehol, S. A. S. & Eide, P. K. Glymphatic MRI in idiopathic normal pressure hydrocephalus. *Brain* **140**, 2691–2705 (2017).
- 467 12. Louveau, A. *et al.* Understanding the functions and relationships of the glymphatic system and meningeal lymphatics. *The J. clinical investigation* **127**, 3210–3219 (2017).
- 468 13. Proulx, S. T. Cerebrospinal fluid outflow: a review of the historical and contemporary evidence for arachnoid villi, perineural routes, and dural lymphatics. *Cell. Mol. Life Sci.* **78**, 2429–2457 (2021).
- 469 14. Bohr, T. *et al.* The glymphatic system: Current understanding and modeling. *iScience* **25**, 104987 (2022).
- 470 15. Ringstad, G. *et al.* Brain-wide glymphatic enhancement and clearance in humans assessed with MRI. *JCI insight* **3** (2018).
- 471 16. Eide, P. K., Valnes, L. M., Lindstrøm, E. K., Mardal, K.-A. & Ringstad, G. Direction and magnitude of cerebrospinal fluid flow vary substantially across central nervous system diseases. *Fluids Barriers CNS* **18**, 1–18 (2021).
- 472 17. Eide, P. K., Pripp, A. H., Ringstad, G. & Valnes, L. M. Impaired glymphatic function in idiopathic intracranial hypertension. *Brain communications* **3**, fcab043 (2021).
- 473 18. Lohela, T. J., Lilius, T. O. & Nedergaard, M. The glymphatic system: implications for drugs for central nervous system diseases. *Nat. Rev. Drug Discov.* **21**, 763–779 (2022).
- 474 19. Kadan-Lottick, N. S. *et al.* Comparison of neurocognitive functioning in children previously randomly assigned to intrathecal methotrexate compared with triple intrathecal therapy for the treatment of childhood acute lymphoblastic leukemia. *J. clinical oncology* **27**, 5986–5992 (2009).
- 475 20. Eide, P. K. *et al.* Clinical application of intrathecal gadobutrol for assessment of cerebrospinal fluid tracer clearance to blood. *JCI insight* **6** (2021).
- 476 21. van Osch, M. J. *et al.* Human brain clearance imaging: Pathways taken by magnetic resonance imaging contrast agents after administration in cerebrospinal fluid and blood. *NMR Biomed.* e5159 (2024).
- 477 22. Rennels, M., Gregory, T. F., Blaumanis, O. R., Fujimoto, K. & Grady, P. A. Evidence for a ‘paravascular’ fluid circulation in the mammalian central nervous system, provided by the rapid distribution of tracer protein throughout the brain from the subarachnoid space. *Brain Res.* **326**, 47–63 (1985).
- 478 23. Zhang, E., Inman, C. & Weller, R. Interrelationships of the pia mater and the perivascular (Virchow-Robin) spaces in the human cerebrum. *J. anatomy* **170**, 111 (1990).
- 479 24. Ichimura, T., Fraser, P. A. & Cserr, H. F. Distribution of extracellular tracers in perivascular spaces of the rat brain. *Brain Res.* (1991).
- 480 25. Carare, R. O. *et al.* Solutes, but not cells, drain from the brain parenchyma along basement membranes of capillaries and arteries: significance for cerebral amyloid angiopathy and neuroimmunology. *Neuropathol. Appl. Neurobiol.* **34**, 131–144 (2008).
- 481 26. Foley, C. P., Nishimura, N., Neeves, K. B., Schaffer, C. B. & Olbricht, W. L. Real-time imaging of perivascular transport of nanoparticles during convection-enhanced delivery in the rat cortex. *Ann. Biomed. Eng.* **40**, 292–303 (2012).
- 482 27. Hannocks, M.-J. *et al.* Molecular characterization of perivascular drainage pathways in the murine brain. *J. Cereb. Blood Flow & Metab.* **38**, 669–686 (2018).
- 483 28. van Veluw, S. J. *et al.* Is CAA a perivascular brain clearance disease? A discussion of the evidence to date and outlook for future studies. *Cell. Mol. Life Sci.* **81**, 239 (2024).
- 484 29. Eide, P. K. & Ringstad, G. Functional analysis of the human perivascular subarachnoid space. *Nat. Commun.* **15**, 2001 (2024).
- 485 30. Yamamoto, E. A. *et al.* The perivascular space is a conduit for cerebrospinal fluid flow in humans: A proof-of-principle report. *Proc. Natl. Acad. Sci. U. S. A.* **121**, e2407246121 (2024).

- 510 31. Hadaczek, P. *et al.* The “perivascular pump” driven by arterial pulsation is a powerful mechanism for the distribution of
511 therapeutic molecules within the brain. *Mol. Ther.* **14**, 69–78 (2006).
- 512 32. Iliff, J. J. *et al.* Cerebral arterial pulsation drives paravascular CSF–interstitial fluid exchange in the murine brain. *J.*
513 *Neurosci.* **33**, 18190–18199 (2013).
- 514 33. Bedussi, B., Almasian, M., de Vos, J., VanBavel, E. & Bakker, E. N. Paravascular spaces at the brain surface: Low
515 resistance pathways for cerebrospinal fluid flow. *J. Cereb. Blood Flow & Metab.* **38**, 719–726 (2018).
- 516 34. Mestre, H. *et al.* Flow of cerebrospinal fluid is driven by arterial pulsations and is reduced in hypertension. *Nat.*
517 *communications* **9**, 4878 (2018).
- 518 35. Boster, K. A. *et al.* Artificial intelligence velocimetry reveals in vivo flow rates, pressure gradients, and shear stresses in
519 murine perivascular flows. *Proc. Natl. Acad. Sci.* **120**, e2217744120 (2023).
- 520 36. Hirschler, L. *et al.* Region specific drivers of cerebrospinal fluid mobility as measured by high-resolution non-invasive
521 MRI in humans. *Res. Sq.* (2024).
- 522 37. Bilston, L. E., Fletcher, D. F., Brodbelt, A. R. & Stoodley, M. A. Arterial pulsation-driven cerebrospinal fluid flow in the
523 perivascular space: a computational model. *Comput. Methods Biomed. Eng.* **6**, 235–241 (2003).
- 524 38. Rey, J. & Sarntinoranont, M. Pulsatile flow drivers in brain parenchyma and perivascular spaces: a resistance network
525 model study. *Fluids Barriers CNS* **15**, 20 (2018).
- 526 39. Daversin-Catty, C., Vinje, V., Mardal, K.-A. & Rognes, M. E. The mechanisms behind perivascular fluid flow. *PLoS One*
527 **15**, e0244442 (2020).
- 528 40. Kedarasetti, R. T. *et al.* Functional hyperemia drives fluid exchange in the paravascular space. *Fluids Barriers CNS* **17**,
529 52 (2020).
- 530 41. Gjerde, I. G., Rognes, M. E. & Sánchez, A. L. The directional flow generated by peristalsis in perivascular net-
531 works—theoretical and numerical reduced-order descriptions. *J. Appl. Phys.* **134** (2023).
- 532 42. Nozaleda, G. L., Coenen, W., Haughton, V. & Sánchez, A. L. Arterial pulsations and transmantle pressure synergetically
533 drive glymphatic flow. *TBA* (2024).
- 534 43. Asgari, M., De Zélicourt, D. & Kurtcuoglu, V. Glymphatic solute transport does not require bulk flow. *Sci. reports* **6**,
535 38635 (2016).
- 536 44. Sharp, K. M., Carare, R. O. & Martin, B. A. Dispersion in porous media in oscillatory flow between flat plates:
537 applications to intrathecal, periarterial and paraarterial solute transport in the central nervous system. *Fluids Barriers*
538 *CNS* **16**, 1–17 (2019).
- 539 45. Thomas, J. H. Fluid dynamics of cerebrospinal fluid flow in perivascular spaces. *J. Royal Soc. Interface* **16**, 20190572
540 (2019).
- 541 46. Kedarasetti, R. T., Drew, P. J. & Costanzo, F. Arterial pulsations drive oscillatory flow of CSF but not directional pumping.
542 *Sci. reports* **10**, 10102 (2020).
- 543 47. Troyetsky, D. E., Tithof, J., Thomas, J. H. & Kelley, D. H. Dispersion as a waste-clearance mechanism in flow through
544 penetrating perivascular spaces in the brain. *Sci. reports* **11**, 4595 (2021).
- 545 48. Martinac, A. D., Fletcher, D. F. & Bilston, L. E. Phase offset between arterial pulsations and subarachnoid space pressure
546 fluctuations are unlikely to drive periarterial cerebrospinal fluid flow. *Biomech. Model. Mechanobiol.* **20**, 1751–1766
547 (2021).
- 548 49. Damkier, H. H., Brown, P. D. & Praetorius, J. Cerebrospinal fluid secretion by the choroid plexus. *Physiol. reviews* **93**,
549 1847–1892 (2013).
- 550 50. Steffensen, A. B. *et al.* Cotransporter-mediated water transport underlying cerebrospinal fluid formation. *Nat. communi-*
551 *cations* **9**, 2167 (2018).
- 552 51. Liu, G. *et al.* Direct measurement of cerebrospinal fluid production in mice. *Cell reports* **33** (2020).
- 553 52. Greitz, D., Franck, A. & Nordell, B. On the pulsatile nature of intracranial and spinal CSF-circulation demonstrated by
554 MR imaging. *Acta Radiol.* **34**, 321–328 (1993).
- 555 53. Wagshul, M. E., Eide, P. K. & Madsen, J. R. The pulsating brain: a review of experimental and clinical studies of
556 intracranial pulsatility. *Fluids Barriers CNS* **8**, 1–23 (2011).

- 557 54. Sweetman, B. & Linninger, A. A. Cerebrospinal fluid flow dynamics in the central nervous system. *Ann. Biomed. Eng.*
558 39, 484–496 (2011).
- 559 55. Fultz, N. E. *et al.* Coupled electrophysiological, hemodynamic, and cerebrospinal fluid oscillations in human sleep. *Science* 366, 628–631 (2019).
- 560 56. Vinje, V. *et al.* Respiratory influence on cerebrospinal fluid flow – a computational study based on long-term intracranial
562 pressure measurements. *Sci. Rep.* 9 (2019).
- 563 57. Causemann, M., Vinje, V. & Rognes, M. E. Human intracranial pulsatility during the cardiac cycle: a computational
564 modelling framework. *Fluids Barriers CNS* 19, 84 (2022).
- 565 58. Williams, S. D. *et al.* Neural activity induced by sensory stimulation can drive large-scale cerebrospinal fluid flow during
566 wakefulness in humans. *PLoS biology* 21, e3002035 (2023).
- 567 59. Zimmermann, J. *et al.* Total cerebral blood volume changes drive macroscopic cerebrospinal fluid flux in humans. *bioRxiv*
568 2023–04 (2023).
- 569 60. Weller, R. O. Microscopic morphology and histology of the human meninges. *Morphologie* 89, 22–34 (2005).
- 570 61. Bedussi, B. *et al.* Paravascular channels, cisterns, and the subarachnoid space in the rat brain: a single compartment with
571 preferential pathways. *J. Cereb. Blood Flow & Metab.* 37, 1374–1385 (2017).
- 572 62. Pizzo, M. E. *et al.* Intrathecral antibody distribution in the rat brain: surface diffusion, perivascular transport and osmotic
573 enhancement of delivery. *The J. physiology* 596, 445–475 (2018).
- 574 63. Mestre, H. *et al.* Periarteriolar spaces modulate cerebrospinal fluid transport into brain and demonstrate altered morphology
575 in aging and Alzheimer's disease. *Nat. Commun.* 13, 3897 (2022).
- 576 64. Møllgård, K. *et al.* A mesothelium divides the subarachnoid space into functional compartments. *Science* 379, 84–88
577 (2023).
- 578 65. Smets, N. G., van der Panne, S. A., Strijkers, G. J. & Bakker, E. N. T. P. Perivascular spaces around arteries exceed
579 perivenous spaces in the mouse brain. *Sci. Rep.* 14, 17655 (2024).
- 580 66. Masri, R., Zeinhofer, M., Kuchta, M. & Rognes, M. E. The modelling error in multi-dimensional time-dependent solute
581 transport models. *ESAIM: Math. Model. Numer. Analysis* 58, 1681–1724 (2024).
- 582 67. Hodneland, E. *et al.* A new framework for assessing subject-specific whole brain circulation and perfusion using
583 MRI-based measurements and a multi-scale continuous flow model. *PLoS computational biology* 15, e1007073 (2019).
- 584 68. Watts, R., Steinklein, J. M., Waldman, L., Zhou, X. & Filippi, C. G. Measuring glymphatic flow in man using quantitative
585 contrast-enhanced MRI. *AJNR Am. J. Neuroradiol.* 40, 648–651 (2019).
- 586 69. Causemann, M., Masri, R., Kuchta, M. & Rognes, M. E. Software and data for "In-silico molecular enrichment and
587 clearance of the human intracranial space", DOI: [10.5281/zenodo.1474916](https://doi.org/10.5281/zenodo.1474916) (2025).
- 588 70. Deistung, A., Dittrich, E., Sedlacik, J., Rauscher, A. & Reichenbach, J. R. ToF-SWI: simultaneous time of flight and
589 fully flow compensated susceptibility weighted imaging. *J. Magn. Reson. Imaging: An Off. J. Int. Soc. for Magn. Reson.
590 Medicine* 29, 1478–1484 (2009).
- 591 71. Schweser, F., Sommer, K., Deistung, A. & Reichenbach, J. R. Quantitative susceptibility mapping for investigating subtle
592 susceptibility variations in the human brain. *Neuroimage* 62, 2083–2100 (2012).
- 593 72. Reichenbach, J. R. The future of susceptibility contrast for assessment of anatomy and function. *Neuroimage* 62,
594 1311–1315 (2012).
- 595 73. Deistung, A., Schweser, F. & Reichenbach, J. R. Overview of quantitative susceptibility mapping. *NMR Biomed.* 30,
596 e3569 (2017).
- 597 74. Smith, A. J. & Verkman, A. S. Going against the flow: Interstitial solute transport in brain is diffusive and aquaporin-4
598 independent. *The J. physiology* 597, 4421 (2019).
- 599 75. Hladky, S. B. & Barrand, M. A. The glymphatic hypothesis: the theory and the evidence. *Fluids Barriers CNS* 19, 9
600 (2022).
- 601 76. Betsholtz, C. *et al.* Advances and controversies in meningeal biology. *Nat. Neurosci.* 1–17 (2024).
- 602 77. Syková, E. & Nicholson, C. Diffusion in brain extracellular space. *Physiol. reviews* 88, 1277–1340 (2008).
- 603 78. Ray, L. A., Pike, M., Simon, M., Iliff, J. J. & Heys, J. J. Quantitative analysis of macroscopic solute transport in the
604 murine brain. *Fluids Barriers CNS* 18, 55 (2021).

- 605 79. Hornkjøl, M. *et al.* CSF circulation and dispersion yield rapid clearance from intracranial compartments. *Front. Bioeng.*
606 *Biotechnol.* **10**, 932469–932469 (2022).
- 607 80. Alnæs, M. *et al.* The FEniCS project version 1.5. *Arch. numerical software* **3** (2015).
- 608 81. Kuchta, M. Assembly of multiscale linear PDE operators. In *Numerical Mathematics and Advanced Applications*
609 *ENUMATH 2019: European Conference, Egmond aan Zee, The Netherlands, September 30-October 4*, 641–650
610 (Springer, 2020).
- 611 82. Balédent, O. Imaging of the cerebrospinal fluid circulation. *Adult hydrocephalus* **256**, 121 (2014).
- 612 83. Gutiérrez-Montes, C. *et al.* Effect of normal breathing on the movement of CSF in the spinal subarachnoid space. *Am. J.*
613 *Neuroradiol.* **43**, 1369–1374 (2022).
- 614 84. Liu, P., Owashi, K., Metanbou, S., Capel, C. & Balédent, O. Using real time phase contrast MRI to investigate CSF
615 oscillations and aqueductal pressure gradients during free breathing. In *ISMRM 2024*, 1189 (2024).
- 616 85. van Veluw, S. J. *et al.* Vasomotion as a driving force for paravascular clearance in the awake mouse brain. *Neuron* **105**,
617 549–561.e5 (2020).
- 618 86. Munting, L. P. *et al.* Spontaneous vasomotion propagates along pial arterioles in the awake mouse brain like stimulus-
619 evoked vascular reactivity. *J. Cereb. Blood Flow Metab.* **43**, 1752–1763 (2023).
- 620 87. Bojarskaite, L. *et al.* Sleep cycle-dependent vascular dynamics in male mice and the predicted effects on perivascular
621 cerebrospinal fluid flow and solute transport. *Nat. communications* **14**, 953 (2023).
- 622 88. Broggini, T. *et al.* Long-wavelength traveling waves of vasomotion modulate the perfusion of cortex. *Neuron* **112**,
623 2349–2367.e8 (2024).
- 624 89. Coenen, W., Zhang, X. & Sánchez, A. Lubrication analysis of peristaltic motion in non-axisymmetric annular tubes. *J.*
625 *Fluid Mech.* **921**, R2 (2021).
- 626 90. Jung, J.-Y., Lee, Y.-B. & Kang, C.-K. Novel technique to measure pulse wave velocity in brain vessels using a fast
627 simultaneous multi-slice excitation magnetic resonance sequence. *Sensors* **21**, 6352 (2021).
- 628 91. Zhang, E., Richards, H., Kida, S. & Weller, R. Directional and compartmentalised drainage of interstitial fluid and
629 cerebrospinal fluid from the rat brain. *Acta neuropathologica* **83**, 233–239 (1992).
- 630 92. Koch, T., Vinje, V. & Mardal, K.-A. Estimates of the permeability of extra-cellular pathways through the astrocyte
631 endfoot sheath. *Fluids Barriers CNS* **20**, 1–18 (2023).
- 632 93. Bown, C. W., Carare, R. O., Schrag, M. S. & Jefferson, A. L. Physiology and clinical relevance of enlarged perivascular
633 spaces in the aging brain. *Neurology* **98**, 107–117 (2022).
- 634 94. Bakker, E. N. T. P. *et al.* Lymphatic clearance of the brain: Perivascular, paravascular and significance for neurodegenerative
635 diseases. *Cell. Mol. Neurobiol.* **36**, 181–194 (2016).
- 636 95. Gokina, N. I., Bevan, R. D., Walters, C. L. & Bevan, J. A. Electrical activity underlying rhythmic contraction in human
637 pial arteries. *Circ. research* **78**, 148–153 (1996).
- 638 96. Vinje, V. *et al.* Human brain solute transport quantified by glymphatic MRI-informed biophysics during sleep and sleep
639 deprivation. *Fluids Barriers CNS* **20**, 62 (2023).
- 640 97. Ulv Larsen, S. M. *et al.* Sleep pressure propels cerebrovascular oscillations while sleep intensity correlates with respiration-
641 and cardiac-driven brain pulsations. *medRxiv* (2024).
- 642 98. von Holstein-Rathlou, S., Petersen, N. C. & Nedergaard, M. Voluntary running enhances glymphatic influx in awake
643 behaving, young mice. *Neurosci. letters* **662**, 253–258 (2018).
- 644 99. Yildiz, S. *et al.* Immediate impact of yogic breathing on pulsatile cerebrospinal fluid dynamics. *Sci. reports* **12**, 10894
645 (2022).
- 646 100. Lundgaard, I. *et al.* Beneficial effects of low alcohol exposure, but adverse effects of high alcohol intake on glymphatic
647 function. *Sci. reports* **8**, 2246 (2018).
- 648 101. Siyahhan, B. *et al.* Flow induced by ependymal cilia dominates near-wall cerebrospinal fluid dynamics in the lateral
649 ventricles. *J. Royal Soc. Interface* **11**, 20131189 (2014).
- 650 102. Billot, B. *et al.* Robust machine learning segmentation for large-scale analysis of heterogeneous clinical brain MRI
651 datasets. *Proc. Natl. Acad. Sci.* **120**, e2216399120 (2023).

- 652 103. Billot, B. *et al.* Synthseg: Segmentation of brain MRI scans of any contrast and resolution without retraining. *Med. image*
653 analysis **86**, 102789 (2023).
- 654 104. Hu, Y., Schneider, T., Wang, B., Zorin, D. & Panozzo, D. Fast tetrahedral meshing in the wild. *ACM Transactions on*
655 *Graph. (TOG)* **39**, 117–1 (2020).
- 656 105. Hladky, S. B. & Barrand, M. A. Regulation of brain fluid volumes and pressures: basic principles, intracranial hypertension,
657 ventriculomegaly and hydrocephalus. *Fluids Barriers CNS* **21**, 57 (2024).
- 658 106. Silversmith, W., Bae, J. A., Li, P. H. & Wilson, A. seung-lab/kimimaro: Zenodo release v1, DOI: [10.5281/zenodo.5539913](https://doi.org/10.5281/zenodo.5539913)
659 (2021).
- 660 107. Taylor, G. I. Dispersion of soluble matter in solvent flowing slowly through a tube. *Proc. Royal Soc. London. Ser. A.*
661 *Math. Phys. Sci.* **219**, 186–203 (1953).
- 662 108. Watson, E. Diffusion in oscillatory pipe flow. *J. Fluid Mech.* **133**, 233–244 (1983).
- 663 109. Nicholson, C. & Phillips, J. Ion diffusion modified by tortuosity and volume fraction in the extracellular microenvironment
664 of the rat cerebellum. *The J. physiology* **321**, 225–257 (1981).
- 665 110. Valnes, L. M. *et al.* Apparent diffusion coefficient estimates based on 24 hours tracer movement support glymphatic
666 transport in human cerebral cortex. *Sci. reports* **10**, 9176 (2020).
- 667 111. Jørgen N. Riseth, K.-A. M., Timo Koch. Two-compartment modeling of tracer transport in the brain. In Rognes,
668 M. E., Vinje, V., Dokken, J., Valnes, L. M. & Mardal, K.-A. (eds.) *MRI2FEM II: from magnetic resonance images to*
669 *computational brain mechanics*, DOI: [xxxx/yyy-zzz](https://doi.org/xxxx/yyy-zzz) (Springer, 2025).
- 670 112. Nilsson, C. *et al.* Circadian variation in human cerebrospinal fluid production measured by magnetic resonance imaging.
671 *Am. J. Physiol. Integr. Comp. Physiol.* **262**, R20–R24 (1992).
- 672 113. Bloomfield, I., Johnston, I. & Bilston, L. Effects of proteins, blood cells and glucose on the viscosity of cerebrospinal
673 fluid. *Pediatr. neurosurgery* **28**, 246–251 (1998).
- 674 114. Ern, A., Stephansen, A. F. & Zunino, P. A discontinuous Galerkin method with weighted averages for advection–diffusion
675 equations with locally small and anisotropic diffusivity. *IMA J. Numer. Analysis* **29**, 235–256 (2009).
- 676 115. Masri, R., Kuchta, M. & Riviere, B. Discontinuous Galerkin methods for 3D–1D systems. *SIAM J. on Numer. Analysis*
677 **62**, 1814–1843 (2024).
- 678 116. Laurino, F. & Zunino, P. Derivation and analysis of coupled PDEs on manifolds with high dimensionality gap arising
679 from topological model reduction. *ESAIM: Math. Model. Numer. Analysis* **53**, 2047–2080 (2019).
- 680 117. Masri, R., Shen, B. & Riviere, B. Discontinuous Galerkin approximations to elliptic and parabolic problems with a Dirac
681 line source. *ESAIM: Math. Model. Numer. Analysis* **57**, 585–620 (2023).
- 682 118. Köppl, T., Vidotto, E. & Wohlmuth, B. A local error estimate for the Poisson equation with a line source term. In
683 *Numerical mathematics and advanced applications ENUMATH 2015*, 421–429 (Springer, 2016).
- 684 119. Hong, Q., Kraus, J., Xu, J. & Zikatanov, L. A robust multigrid method for discontinuous Galerkin discretizations of
685 Stokes and linear elasticity equations. *Numer. Math.* **132**, 23–49 (2016).
- 686 120. Cesmelioglu, A. & Rhebergen, S. A compatible embedded-hybridized discontinuous Galerkin method for the Stokes-
687 Darcy-transport problem. *Commun. on Appl. Math. Comput.* **4**, 293–318 (2022).

688 Acknowledgments

689 All authors express their gratitude to Prof. Jürgen Reichenbach for generously sharing the multi-modal human MR data, and to
690 Prof. Erlend Hodneland for facilitating this data exchange. The authors also thank Profs. Per Kristian Eide, Geir Ringstad and
691 Rune Enger for valuable input and discussions. M.E.R. acknowledges support from Stiftelsen Kristian Gerhard Jebsen via the
692 K. G. Jebsen Centre for Brain Fluid Research. M.C., R.M., and M.E.R. acknowledge support from the Research Council of
693 Norway (RCN) via grant #324239 (EMIx). Simulations were performed on the Experimental Infrastructure for Exploration of
694 Exascale Computing (eX3), which is financially supported by the RCN under contract 270053. M.K. acknowledges support
695 from the RCN grant #303362. The figures 1A, 1D, 2C, 3C, 5A and 6A were created in Biorender.

696 Author contributions statement

697 M.C., M.K, R.M., and M.E.R. conceived and designed the project. M.C., M.K, R.M., and M.E.R. contributed to software
698 development. M.C., M.K, and R.M. conducted the experiments. M.C. analyzed the results and prepared the figures. M.C.,
699 M.K., R.M and M.E.R wrote the manuscript. All authors edited and reviewed the manuscript.

700 **Competing interests**

701 The authors declare no competing interests.